Received: Added at production | Revised: Added at production | Accepted: Added at production

DOI: xxx/xxxx

RESEARCH ARTICLE

A semi-hybrid-mixed method for Stokes-Brinkman-Darcy flows with H(div)-velocity fields

Pablo G. S. Carvalho*[1] | Philippe R.B. Devloo[2] | Sônia M. Gomes[3]

[1]ICMC, Universidade de São Paulo, São Carlos, SP, Brazil
[2]FECFAU, Universidade Estadual de Campinas, Campinas, SP, Brazil
[3]IMECC, Universidade Estadual de Campinas, Campinas, SP, Brazil

Correspondence
*Pablo Giovanni Silva Carvalho, Instituto de Ciências Matemáticas e de Computação, Universidade de São Paulo, Av. Trabalhador São-carlense, 400, 13566-590, São Carlos, SP, Brazil. Email: pablogscarvalho@usp.br

Summary

We consider new semi-hybrid-mixed finite element formulations for Stokes-Brinkman problems. Using **H**(div)-conforming approximate velocity fields, the continuity of normal components over element interfaces is taken for granted, and pressure is searched in discontinuous spaces preserving the divergence compatibility property. Tangential continuity is weakly imposed by a Lagrange multiplier playing the role of tangential traction. The method is strongly mass-conservative, leading to exact divergence-free simulations of incompressible flows. The Lagrange multiplier space requires specific choices according to the velocity approximations implemented in each element geometry. In certain cases, classic divergence-compatible pairs adopted for Darcy flows may require divergence-free bubble enrichment to enforce tangential continuity in some extent, avoiding any extra stabilization technique. Considerable improvement in computational performance is achieved by the application of static condensation: the global system is solved only for a piecewise constant pressure variable, velocity normal trace and tangential traction over interfaces. The remaining solution components are recovered by solving independent local Neumann problems in each element. Numerical results are presented for a set of standard test cases in the field of Stokes-Brinkman-Darcy flows with known analytical solutions. The main convergence properties of the method are verified in the whole range of parameters, from Stokes to Darcy limits, as well as for the combined Stokes-Darcy scenario. The robustness of the method is also demonstrated for more challenging test problems with complex non-conforming meshes with local refinement patterns as well as for curved geometry.

KEYWORDS:
Hybrid-mixed method, Stokes flow, Darcy's law, Divergence-free, Static condensation.

1 | INTRODUCTION

Fluid mechanics modeling has been the subject of different computational and experimental investigations, with a variety of applications in science and engineering. Our focus is on a finite element (FE) numerical approach for the fundamental Stokes, Brinkman and Darcy models for incompressible fluid flows. For instance, they are usually applied in modeling flow through rough-walled rocks, fractures and small cavities in porous media, called "vugs", and also appear in surface-water hydrology, filtration and lubrication problems [1].

Stokes and Brinkman problems consider fluid flows occupying a region Ω, with constant viscosity $\mu > 0$, boundary Dirichlet datum $\boldsymbol{u}_D \in H^{1/2}(\partial\Omega_D, \mathbb{R}^d)$. When the case is $\Omega_D = \Omega$, we assume the compatibility condition $\int_{\partial\Omega} \boldsymbol{u}_D \cdot \boldsymbol{n}^\Omega \, ds = 0$ (here $\boldsymbol{n}^\Omega$ denotes the outward unit normal vector on $\partial\Omega$). The constitutive equation $\boldsymbol{\sigma} = \boldsymbol{\sigma}(\boldsymbol{u}, p) = 2\mu \, D(\boldsymbol{u}) - pI$ holds for the flow stress tensor, where $D(\boldsymbol{u}) = \frac{1}{2}(\nabla \boldsymbol{u} + \nabla \boldsymbol{u}^T)$ is the symmetric gradient tensor. Both cases can be formulated in a unified form, in terms of the velocity $\boldsymbol{u}$ and pressure p fields, by the system of momentum balance and conservation of mass equations

$$-\underline{\nabla} \cdot \boldsymbol{\sigma}(\boldsymbol{u}, p) + \alpha \boldsymbol{u} = \boldsymbol{f} \quad \text{in} \quad \Omega, \tag{1}$$

$$\nabla \cdot \boldsymbol{u} = 0 \quad \text{in} \quad \Omega, \tag{2}$$

$$\boldsymbol{u} = \boldsymbol{u}_D \quad \text{on} \quad \partial\Omega_D, \tag{3}$$

$$\boldsymbol{\sigma} \boldsymbol{n} = 0 \quad \text{on} \quad \partial\Omega_N, \tag{4}$$

where $\boldsymbol{f} \in L^2(\Omega, \mathbb{R}^d)$ is a force term. Brinkman problems occur for $\alpha > 0$ defining a dynamic viscosity divided by the permeability. The Stokes problem is the limit case when $\alpha = 0$. Observe that the model can also be interpreted as a Darcy problem with Neumann boundary condition in the limit case $\mu = 0$ with $\boldsymbol{f} \equiv 0$.

The goal of this study is to propose, analyze and implement a new hybrid-mixed nonconforming formulation for problem (1)-(4) using divergence-compatible FE pairs in $\mathrm{H(div}, \Omega)\times\mathrm{L}^2(\Omega)$ for velocity and pressure discretizations. The velocity normal trace continuity is taken for granted, and requirement for continuous tangential velocity components is weakened but not removed completely from the approximation spaces (as it is done in full DG methods). Given a geometric partition $\mathcal{T} = \{K\}$ of the flow domain, a new tangential traction variable (Lagrange multiplier) is introduced over the facets of the mesh skeleton $\mathcal{E}$ (edges or faces of element boundaries). In this sense, a semi-hybridization is applied. Well-posedness of the method holds with proper choices of the FE space for the Lagrange multiplier avoiding the modification of the formulation with extra stabilization treatment. An error analysis reveals typical estimates held by nonconforming methods for these problems.

There exist in the literature several FE discretizations for this mathematical model[2]. For the Stokes problem, a usual approach is based on a mixed variational formulation, having the velocity of the fluid as primary variable, with continuous traces over element interfaces. It can be characterized as the solution of a constrained minimization problem, where discontinuous pressure fields play the role of a Lagrange multiplier to impose the incompressibility constraint. The main difficulty faced by Stokes H^1-conforming mixed FE models, using continuous velocity fields, occurs in the treatment of the divergence-free condition. For well-posedness, velocity and pressure approximation spaces should verify a rather strict compatibility property, the well known LBB or inf-sup condition[3,4]. For example, the use of equal order Lagrangian elements for both velocity and pressure gives unstable approximations.

To relax this constraint, a variety of nonconforming velocity-pressure mixed methods have been proposed, violating the inter-element continuity condition of the velocity fields to some extent. Let us recall some lines of investigations on this topic, remarking that giving a detailed account of related literature lies out of the scope of the present work.

- In the classic seminal work by Crouzeix-Raviart[5], the principle is to take velocities that are only continuous at appropriate Gauss points on triangle edges. A general theory for analyzing nonconforming methods applied to Stokes problems can also be found in this publication. We refer to[6] for a survey review on this matter.

- Discontinuous Galerkin (DG) methodology discretizes the variables in full broken spaces based on a partition of Ω, without assuming any continuity constraint in the approximation spaces[7,8,9]. As requested in these classical DG FE methods, extra stabilization terms are incorporated to the variational formulation in order to have stable and accurate simulations. Recently[10], new DG methods for Brinkman and coupled Brinkman-Darcy problems have been proposed based in staggered meshes, which are free of stabilization terms and yield strongly conservative results.

- Nonconforming approaches in between H^1-conforming FE methods and full DG methods use divergence-compatible FE pairs in $\mathrm{H(div}, \Omega) \times \mathrm{L}^2(\Omega)$ for velocity and pressure discretizations. Namely, the approximate velocity fields are assumed from start to have continuous normal traces across element interfaces. In this direction, in the semi-DG proposals[11,12], for Stokes and Brinkman problems, respectively, the penalization is introduced just on the velocity tangential components over element interfaces. We refer to[13] for a unified representation and a comparative study of some known full DG and semi-DG schemes for Stokes, as well for Brinkman and coupled Stokes-Darcy problems.

  Penalization can be avoided when divergence-compatible FE pairs in $\mathrm{H(div}, \Omega) \times \mathrm{L}^2(\Omega)$ are adopted, but the enforcement of some kind of tangential continuity is needed. For that, the velocity FE space is enriched with some properly chosen divergence-free bubble velocity FE of higher degree. The original pressure space is maintained, without spoiling the

divergence consistency property. In this direction, we refer to [14,15,16,17] for methods based on simplexes and to [18,19] for quadrilateral and hexahedral meshes. Excepting [17], all these methods are of lowest order.

- Another class of nonconforming methods occurs by hybridization: by relaxing the velocity continuity between elements of a domain partition, an appropriate Lagrange multiplier is introduced to weakly impose it. The term hybrid comes from this additional variable used for the approximation of fields over the skeleton of the partition. In the context of structural mechanics, the importance of hybridization was recognized since the beginning of FE history, and originally presented in [20]. Since then, these principles have been widely explored in the design of new formulations in many fields, motivated by the growing interest in solving high precision problems with optimized computational processes. For them, model resolution is divided into local independent problems, favoring parallel computing implementations, and profiting from static condensation techniques (e.g., see [21]). Moreover, when the Lagrange multiplier field admits a physical interpretation, giving further information about the solution, it can be exploited in a post-process to improve accuracy and/or for a posteriori error analysis. Following the "divide-and-conquer" principle, hybrid formulations for Stokes and/or Brinkman problems have been proposed in the literature using different approaches.

  There are the so called Hybrid Discontinuous Galerkin methods (HDG). In addition to velocity and pressure, the technique has been developed by the incorporation of vorticity, velocity gradient or stress variables. The local variables are piecewisely defined by polynomials of the same degree for all the components of the approximate solution, and solved globally for the coupled condensed systems for the approximate trace of the velocity over interfaces and the mean of the pressure on the elements. The local solvers approximate the remaining field components in terms of the numerical trace of the velocity and the mean of pressure. Divergence-free and $\boldsymbol{H}(\mathrm{div})$-conformity properties require a post-processed velocity. We refer the reader to the survey in HDG [22] for the specific case of Stokes problems.

  The hybrid DG method for the Stokes problem in the velocity-pressure format introduced and analyzed in [23] adopts Lagrange multipliers associated with the trace of the velocity field. Other variants of this method are considered for the Stokes [24,25,26] and Stokes-Darcy [27] problems, with Lagrange multipliers for both velocity and pressure traces. With properly chosen FE space configurations for velocity, pressure and trace variables, the later methods can be local mass conservative and deliver pointwise divergence-free fields.

  The method considered in [28], in the so called Hybrid High-Order (HHO) context, is formulated in terms of face-based and internal degrees of freedom in each element. The variational formulation takes into account a velocity reconstruction operator on a polynomial space of higher degree, and requires the adoption of reconstruction operators.

  For the sake of well posedness, all the aforementioned hybrid methods require the incorporation in the equations of extra stabilization terms.

As listed in the sequel, the semi-hybrid-mixed formulation proposed in this study shares the main characteristics of other hybrid methods, specially with respect to the MHM multiscale hybrid mixed method (MHM) proposed in [29] for the Stokes-Brinkman problem. However, the use divergence-compatible FE pairs in $\mathrm{H}(\mathrm{div},\Omega)\times\mathrm{L}^2(\Omega)$ for velocity and pressure discretizations offers some additional positive properties.

1. Assuming $\boldsymbol{u}\in\boldsymbol{H}(\mathrm{div},\Omega)$ and decomposing the domain Ω by a partition $\mathcal{T}=\{K\}$, hibridization occurs by weakly enforcing the tangential continuity by the action of a tangential traction Lagrange multiplier. Inspired by the full-hybrid mixed formulation in [29], the new proposed method can be interpreted as a discrete version of a semi-hybrid mixed variational formulation for the problem in infinite dimension (which is proved to be equivalent to the classic mixed formulation for $\boldsymbol{u}\in\boldsymbol{H}^1(\Omega)$).

2. The method is strongly locally conservative and naturally gives exact divergence-free velocity fields. Robustness with respect to pressure-consistency and to viscosity in the limiting case of Darcy flows is observed. As discussed in the survey [30], few schemes can achieve these properties simultaneously.

3. A static-condensation scheme can be applied, by taking the Lagrange multiplier, the velocity normal trace over element interfaces, and the piecewise constant element-average pressure as primary variables, given by the unique solution of a global system of equations. The remaining velocity and pressure degrees of freedom are secondary variables. They are recovered by solving local Neumann problems restricted to each element K.

4. The method allows efficient parallel implementations since the degrees of freedom on the element boundary are located at the facets (edges or faces) such that the local communication of common data affects at most two elements.

5. The coupling of Stokes, Brinkman and porous media flows can be implemented naturally.

Outline of the paper

After some preliminary comments concerning notation and the adopted functional framework, we describe three equivalent mixed formulations for the model problem, with different continuity of velocity traces. Namely, In Section 2.3 there is the classic mixed formulation for continuous traces on interfaces, the full hybrid-mixed variational formulation for discontinuous traces, and the new semi-hybrid-mixed variant assuming continuous normal traces. FE discretizations for this semi-hybrid-mixed method are proposed in Section 3. They are based on divergence-compatible FE pairs for approximate velocity and pressure fields. We describe the additional trace compatibility conditions on the FE spaces required for solution existence and uniqueness. We also discuss convergence issues for the method. In the sequel, the focus in Section 4 is on some specific examples of FE space configurations using classic divergence-compatible FE pairs based on triangular, quadrilateral, tetrahedral or hexahedral meshes, for which the trace compatibility property is documented. The hybridization of a class of stable nonconforming methods proposed in the literature is also illustrated.

Section 5 is dedicated to the description of some important aspects in computational implementation and of the proposed static-condensation procedure for the semi-hybrid-mixed finite element method. Simulation results for a set of standard test cases in the field of Stokes-Brinkman-Darcy flows with known analytical solutions integrate Section 6 for the verification of predicted convergence rates, velocity divergence-free and pressure robustness properties. Comparison of convergence histories is also presented with respect to numerical results obtained by some DG methods published previously on the same subject. Moreover, the robustness of the method is also demonstrated for more challenging tests with more complex geometry. In Section 7, the semi-hybrid-mixed method for the coupled Stokes-Darcy scenario is formulated, numerically verified for convergence, and applied to a carbonate karst reservoir.

2 | WEAK FORMULATIONS FOR THE MODEL PROBLEM

We introduce some basic notation and recall some variational formulations for the model problem: the classic mixed method and the mixed method of current interest, combined with hybridization. We assume pure Dirichlet boundary condition $\partial\Omega_D = \partial\Omega$. The simple cases involving Neumann boundary conditions, without the pressure zero mean solvability constraint, shall be treated in the numerical applications as well.

2.1 | Comments about notation

Let $\Omega \subset \mathbb{R}^d$, $d \in \{2, 3\}$, be a connected polyhedral domain. Variational formulations shall be presented here as subordinated to a partition $\mathcal{T} = \{K\}$ of Ω, K having one of the usual element geometry. The set Γ formed by all element facets E (edges in 2D or faces in 3D) is called the mesh skeleton, and $\mathring{\Gamma} = \{E \in \Gamma : E \subset \Omega\}$ denotes the set of internal facets. Over Γ, once and for all, a vector field $\boldsymbol{n}$ is fixed such that $\boldsymbol{n}|_E$ is a unit normal associated to the facet $E \in \Gamma$, such that $\boldsymbol{n} = \boldsymbol{n}^\Omega$ for facets over $\partial\Omega$.

Throughout the text, for any subregion $D \subseteq \Omega$, denote by $\boldsymbol{n}^D$ the external unitary normal to ∂D. The scalar Hilbert spaces $L^2(D)$ and $H^s(D)$ and norms $\|\cdot\|_{L^2(D)}$ and $\|\cdot\|_{H^s(D)}$ have the usual meaning. The L^2-inner product is denoted by $(.,.)_D$, and $L^2_0(D)$ stands for the space of functions $\psi \in L^2(D)$ with zero mean value, i.e., $(\psi, 1)_D = 0$. Associated spaces $L^2(D, \mathbb{Z})$ and $H^s(D, \mathbb{Z})$ shall also be considered, taking values in either $\mathbb{Z} = \mathbb{R}^d$ or in matrix spaces $\mathbb{Z} = \mathbb{M} = \mathbb{R}^{d\times d}$. These spaces inherit the corresponding norms associated to the inner products in $L^2(D)$ and $H^s(D)$. The space $H(\mathrm{div}, D)$ denotes the square-integrable vector functions, taking values in $\mathbb{R}^d$, for which the divergence is also square integrable, and $H_0(\mathrm{div}, D) = \{\boldsymbol{v} \in H(\mathrm{div}, D); \boldsymbol{v}\cdot\boldsymbol{n}^D = 0\}$. Similarly, we shall consider tensor functions in $H(\mathrm{div}, D, \mathbb{M})$, recalling that for $\boldsymbol{\sigma} \in H(\mathrm{div}, D, \mathbb{M})$ the divergence $\underline{\nabla}\cdot\boldsymbol{\sigma}$ is the vector field obtained by taking the divergence of each row. These spaces inherit the corresponding norms associated to the inner products $(.,.)_D$ in $L^2(D, \mathbb{R}^d)$, and $L^2(D, \mathbb{M})$. The notation $\langle\ ,\ \rangle_{\partial D}$ defines the duality pairing between the

two function spaces

$$H^{1/2}(\partial D, \mathbb{R}^d) = \left\{ \boldsymbol{\nu} = \boldsymbol{u}|_{\partial D},\ \boldsymbol{u} \in H^1(D, \mathbb{R}^d) \right\},$$
$$H^{-1/2}(\partial D, \mathbb{R}^d) = \left\{ \boldsymbol{\eta} = \boldsymbol{\sigma}\, \boldsymbol{n}^D,\ \boldsymbol{\sigma} \in H(\mathrm{div}, D, \mathbb{M}) \right\}.$$

The subscript D will be dropped if $D = \Omega$. We also denote $\langle \boldsymbol{\eta}, \boldsymbol{\nu} \rangle_{\partial\mathcal{T}} = \sum_{K\in\mathcal{T}} \langle \boldsymbol{\eta}, \boldsymbol{\nu} \rangle_{\partial K}$.

We set $\Psi = L^2(\Omega) = \bar{\Psi} \oplus \Psi^{\perp}$, where $\bar{\Psi} \subset \Psi$ denotes the piecewise constant functions based on $\mathcal{T}$, and $\Psi^{\perp}$ is its L^2-orthogonal complement in Ψ (i.e., of piecewise zero-mean functions over $K \in \mathcal{T}$). Moreover, consider $\Psi_0 = L^2_0(\Omega)$. To relax the constraint of interelement continuity, we introduce the spaces

$$\mathbf{V} = H^1(\mathcal{T}, \mathbb{R}^d) = \left\{ \boldsymbol{v} \in L^2(\Omega, \mathbb{R}^d) :\ \boldsymbol{v}|_K \in H^1(K, \mathbb{R}^d),\ \forall K \in \mathcal{T} \right\}$$
$$\boldsymbol{X} = \mathbf{V} \cap H(\mathrm{div}, \Omega).$$

A direct sum decomposition $\boldsymbol{X} = \boldsymbol{X}^{\partial} + \mathring{\boldsymbol{X}}$ holds in terms of bubble velocity functions $\mathring{\boldsymbol{X}} = \{\mathring{\boldsymbol{v}} \in \boldsymbol{X};\ \mathring{\boldsymbol{v}} \cdot \boldsymbol{n}|_{\partial K} = 0,\ \forall K \in \mathcal{T}\}$, whilst $\boldsymbol{X}^{\partial}$ denotes a complementary space of velocity fields with some sort of non-vanishing normal trace on element boundaries.

Hybridization requires stress trace spaces defined over the mesh skeleton

$$\boldsymbol{\Lambda} = \left\{ \boldsymbol{\sigma}\boldsymbol{n}|_{\partial K} \in H^{-1/2}(\partial K, \mathbb{R}^d),\ \forall K \in \mathcal{T} :\ \boldsymbol{\sigma} \in H(\mathrm{div}, \Omega, \mathbb{M}) \right\}.$$

A direct decomposition $\boldsymbol{\Lambda} = \boldsymbol{\Lambda}^n + \boldsymbol{\Lambda}^t$ holds in terms of normal and tangential components

$$\boldsymbol{\Lambda}^n = \{ \lambda^n = (\lambda \cdot \boldsymbol{n})\boldsymbol{n},\ \lambda \in \boldsymbol{\Lambda} \}, \quad \boldsymbol{\Lambda}^t = \left\{ \lambda^t = \lambda - (\lambda \cdot \boldsymbol{n})\boldsymbol{n},\ \lambda \in \boldsymbol{\Lambda} \right\}.$$

The spaces $\mathbf{V}$ (and and also $\boldsymbol{X}$) are provided with the broken H^1-norm $\|\cdot\|_{1,\mathcal{T}}$ associated to the inner product $(\boldsymbol{u}, \boldsymbol{v})_{1,\mathcal{T}} = (\boldsymbol{u}, \boldsymbol{v}) + \sum_{K\in\mathcal{T}} (\nabla \boldsymbol{u}, \nabla \boldsymbol{v})_K$.

As for $\lambda \in \boldsymbol{\Lambda}$, the dual norm $\|\lambda\|_{\boldsymbol{\Lambda}} = \sup_{\boldsymbol{v}\in\mathbf{V}} \frac{\langle \lambda, \boldsymbol{v} \rangle_{\partial\mathcal{T}}}{\|\boldsymbol{v}\|_{1,\mathcal{T}}}$ is used. Notice that, when restricted to $\lambda^t \in \boldsymbol{\Lambda}^t$, this norm can be equivalently stated as $\|\lambda^t\|_{\boldsymbol{\Lambda}} = \sup_{\boldsymbol{v}\in\boldsymbol{X}} \frac{\langle \lambda^t, \boldsymbol{v} \rangle}{\|\boldsymbol{v}\|_{1,\mathcal{T}}}$.

The following characterization result for $H^1_0(\Omega, \mathbb{R}^d)$ as a subspace of $\boldsymbol{X}$ holds as a direct consequence of [29, Lemma 4].

Lemma 1. A continuous linear functional L on the space $\boldsymbol{X}$ vanishes on $H^1_0(\Omega, \mathbb{R}^d)$ if and only if there exists a unique element $\lambda^t \in \boldsymbol{\Lambda}^t$ such that $L(\boldsymbol{v}) = \langle \boldsymbol{\eta}^t, \boldsymbol{v} \rangle_{\partial\mathcal{T}},\ \boldsymbol{v} \in \boldsymbol{X}$. In other words, $H^1_0(\Omega, \mathbb{R}^d) = \{\boldsymbol{v} \in \boldsymbol{X}; \langle \boldsymbol{\eta}^t, \boldsymbol{v} \rangle_{\partial\mathcal{T}} = 0, \forall \boldsymbol{\eta}^t \in \boldsymbol{\Lambda}^t\}$.

We will frequently use the notation $x \lesssim y$ for the cases that $x \leq cb$ with leading constant independent of discretization parameters.

2.2 | Mixed and hybrid-mixed formulations for Stokes and Brinkman problems

In this section we summarize some mixed and hybrid formulations for the Stokes-Brinkman problem (1)-(3). The classic weak formulation expressed in the mixed form is: find $\boldsymbol{u} \in H^1(\Omega, \mathbb{R}^d)$, $\boldsymbol{u} = \boldsymbol{u}_D$ in $\partial\Omega$, and $p \in \Psi_0$, such that

$$a(\boldsymbol{u}, \boldsymbol{v}) - b(\boldsymbol{v}, p) = (\boldsymbol{f}, \boldsymbol{v}), \quad \forall \boldsymbol{v} \in H^1_0(\Omega, \mathbb{R}^d), \tag{5}$$
$$b(\boldsymbol{u}, q) = 0, \qquad \forall q \in \Psi_0, \tag{6}$$

where the bilinear forms are $a(\boldsymbol{w}, \boldsymbol{v}) = (2\mu D(\boldsymbol{w}), D(\boldsymbol{v})) + \alpha(\boldsymbol{w}, \boldsymbol{v})$ and $b(\boldsymbol{v}, p) = (\nabla \cdot \boldsymbol{v}, p)$. We observe from the assumption $\boldsymbol{f} \in L^2(\Omega, \mathbb{R}^d)$ that $\boldsymbol{\sigma} \in H(\mathrm{div}, \mathbb{M})$. Notice that in Darcy limit ($\mu = 0$ and $\boldsymbol{f} \equiv 0$) $H^1(\Omega, \mathbb{R}^d)$ is not the appropriate space for $\boldsymbol{u}$, and it should be replaced by $H(\mathrm{div}, \Omega)$.

There is another mixed formulation counterpart, which is combined with hybridization. It is based on the broken space setting $\mathbf{V} \times \Psi \times \boldsymbol{\Lambda}$, and use the bilinear forms

$$a_{\mathcal{T}}(\boldsymbol{u}, \boldsymbol{v}) = \sum_{K\in\mathcal{T}} (2\mu D(\boldsymbol{u}), D(\boldsymbol{v}))_K + (\alpha \boldsymbol{u}, \boldsymbol{v}), \quad b_{\mathcal{T}}(\boldsymbol{v}, p) = \sum_{K\in\mathcal{T}} (\nabla \cdot \boldsymbol{v}, p)_K.$$

This hybrid-mixed formulation searches for $(\boldsymbol{u}, p, \lambda, \rho) \in \mathbf{V} \times \Psi \times \boldsymbol{\Lambda} \times \mathbb{R}$ such that

$$a_{\mathcal{T}}(\boldsymbol{u}, \boldsymbol{v}) - b_{\mathcal{T}}(\boldsymbol{v}, p) + \langle \lambda, \boldsymbol{v} \rangle_{\partial\mathcal{T}} = (\boldsymbol{f}, \boldsymbol{v}), \qquad \forall \boldsymbol{v} \in \mathbf{V}, \tag{7}$$
$$b_{\mathcal{T}}(\boldsymbol{u}, q) + (\rho, q) = 0, \qquad \forall q \in \Psi, \tag{8}$$
$$\langle \boldsymbol{\eta}, \boldsymbol{u} \rangle_{\partial\mathcal{T}} = \langle \boldsymbol{\eta}, \boldsymbol{u}_D \rangle, \quad \forall \boldsymbol{\eta} \in \boldsymbol{\Lambda}, \tag{9}$$
$$(\xi, p) = 0, \qquad \forall \xi \in \mathbb{R}. \tag{10}$$

The new variable λ plays the role of Lagrange multiplier to weakly enforce the velocity continuity over $\mathring{\Gamma}$ and the boundary condition, while ρ is introduced to enforce the pressure zero-mean constraint (10).

As proved in [29], these two mixed formulations are equivalent in the following sense.

Theorem 1. The function $(\boldsymbol{u}, p) \in H^1(\Omega, \mathbb{R}^d) \times L^2_0(\Omega)$ is the unique solution of the standard weak formulation (5)-(6) if and only if $(\boldsymbol{u}, p, \lambda, 0) \in \mathbf{V} \times \Psi \times \mathbf{\Lambda} \times \mathbb{R}$ is the unique solution of the hybrid-mixed formulation (7)-(10), for

$$\lambda|_E = -\boldsymbol{\sigma}\boldsymbol{n}|_E, \quad \forall E \in \Gamma,$$

where $\boldsymbol{\sigma} = \boldsymbol{\sigma}(\boldsymbol{u}, p) = 2\mu\, D(\boldsymbol{u}) - p$.

2.3 | Semi-hybrid-mixed formulation for velocity fields in $\mathbf{H}(\mathrm{div}, \Omega)$

Our focus is on a variant of the hybrid-mixed formulation (7)-(10). The principle is to assume, from start, velocity fields with continuous normal traces across element interfaces, i.e. $\boldsymbol{u} \in \boldsymbol{X}$. In this sense, the continuity requirement of the classic H^1-conforming mixed formulation is weakened in this nonconforming method, but it is stronger than in fully discontinuous methods, as for the hybrid-mixed formulation ($\mathbf{u} \in H^1(\mathcal{T}, \mathbb{R}^d)$). As shall be verified, the three approaches give the same solution. Differences appear in their FE discretizations.

For that, firstly observe that $\|\boldsymbol{v}\|_{a_\tau} := a_\mathcal{T}(\boldsymbol{v}, \boldsymbol{v})^{1/2}$ defines a norm in $\boldsymbol{X}$. It is clearly true for Brinkman problems. In the Stokes limit, suppose that, for some $\boldsymbol{v} \in \boldsymbol{X}$, $a_\mathcal{T}(\boldsymbol{v}, \boldsymbol{v}) = \sum_{K\in\mathcal{T}}(2\mu D(\boldsymbol{v}), D(\boldsymbol{v}))_K = 0$. Then $\boldsymbol{v}$ is piecewise defined by rigid body motions, i.e. $D(\boldsymbol{v})|_K = 0$ over $K \in \mathcal{T}_h$, which is not possible for fields $\boldsymbol{v} \neq 0$ in $H(\mathrm{div}, \Omega)$. It is also clear that $b_\mathcal{T}(\boldsymbol{v}, p) = b(\boldsymbol{v}, p)$. Moreover, the traction variable $\lambda \in \mathbf{\Lambda}$ can be expressed as $\lambda = \lambda^n + \lambda^t$ in terms of its normal and tangential components: $\lambda^n = (\lambda \cdot \boldsymbol{n})\boldsymbol{n}$, $\lambda^t = \lambda - \lambda^n \in \mathbf{\Lambda}^t$. Thus, $\langle \lambda, \boldsymbol{v}\rangle_{\partial\mathcal{T}} = \langle \lambda^n, \boldsymbol{v}\rangle_{\partial\mathcal{T}} + \langle \lambda^t, \boldsymbol{v}\rangle_{\partial\mathcal{T}} = \langle \lambda^t, \boldsymbol{v}\rangle_{\partial\mathcal{T}}$ holds for $\boldsymbol{v} \in \boldsymbol{X}$.

By setting $\mathcal{S} = \boldsymbol{X}\times\Psi\times\mathbf{\Lambda}^t$, we may consider the alternative semi-hybrid mixed formulation: find $(\boldsymbol{u}, p, \lambda^t, \rho) \in \mathcal{S}\times\mathbb{R}$ such that

$$a_\mathcal{T}(\boldsymbol{u}, \boldsymbol{v}) - b(\boldsymbol{v}, p) + \langle \lambda^t, \boldsymbol{v}\rangle_{\partial\mathcal{T}} = (\boldsymbol{f}, \boldsymbol{v}), \qquad \forall \boldsymbol{v} \in \boldsymbol{X}, \tag{11}$$

$$b(\boldsymbol{u}, q) + (\rho, q) = 0, \qquad \forall q \in \Psi, \tag{12}$$

$$\langle \boldsymbol{\eta}^t, \boldsymbol{u}\rangle_{\partial\mathcal{T}} = \langle \boldsymbol{\eta}^t, \boldsymbol{u}_D\rangle, \quad \forall \boldsymbol{\eta}^t \in \mathbf{\Lambda}^t, \tag{13}$$

$$(\xi, p) = 0, \qquad \forall \xi \in \mathbb{R}. \tag{14}$$

Theorem 2. The function $(\mathbf{u}, p, \lambda, 0) \in \mathbf{V} \times \Psi \times \mathbf{\Lambda} \times \mathbb{R}$ is the unique solution of the hybrid-mixed formulation (7)-(10) if and only if $(\boldsymbol{u}, p, \lambda^t, 0) \in \mathcal{S} \times \mathbb{R}$ solves the semi-hybrid-mixed formulation (11)-(14), λ^t being the tangential component of λ.

Proof. For comparison, we adopt the momentaneous notation $(\hat{\boldsymbol{u}}, \hat{p}, \hat{\lambda}^t, \hat{\rho}) \in \mathcal{S} \times \mathbb{R}$ for a solution of the semi-hybrid-mixed formulation (11)-(14). Expressing $\boldsymbol{\eta} = \boldsymbol{\eta}^t + \boldsymbol{\eta}^n \in \mathbf{\Lambda}$, equations (9) and (13) imply that $\langle \boldsymbol{\eta}, \mathbf{u} - \hat{\mathbf{u}}\rangle_{\partial\mathcal{T}} = \langle \boldsymbol{\eta}, \mathbf{u}\rangle_{\partial\mathcal{T}} - \langle \boldsymbol{\eta}^t, \hat{\boldsymbol{u}}\rangle_{\partial\mathcal{T}} = 0$, $\forall \lambda \in \mathbf{\Lambda}$. Thus, by Lemma 4 in [29], $\mathbf{u} - \hat{\boldsymbol{u}} \in H^1_0(\Omega, \mathbb{R}^d)$. That is, $\hat{\mathbf{u}} \in H^1(\Omega, \mathbb{R}^d)$ and $\hat{\boldsymbol{u}}|_{\partial\Omega} = u_D$. Taking any $q \in \Psi_0$ in equations (8) and (12), we obtain that $b_\mathcal{T}(\boldsymbol{u} - \hat{\boldsymbol{u}}, q) + (\rho - \hat{\rho}, q) = b(\boldsymbol{u} - \hat{\boldsymbol{u}}, q) = 0$. Moreover, equations (10) and (14) mean that $p - \hat{p} \in \Psi_0$, and choosing any $\boldsymbol{v} \in H^1_0(\Omega, \mathbb{R}^d)$ in equations (7) and (11) we obtain $a(\boldsymbol{u} - \hat{\boldsymbol{u}}, \boldsymbol{v}) + b(\boldsymbol{v}, p - \hat{p}) = 0$. Consequently $\boldsymbol{u} - \hat{\boldsymbol{u}}$ and $p - \hat{p}$ give the unique classic solution of the weak formulation (5)-(6) with homogeneous data $\boldsymbol{f} = 0$ and $\mathbf{u}_D = 0$. That is, $\boldsymbol{u} = \hat{\boldsymbol{u}}$ and $p = \hat{p}$. For constant test function $q = \hat{\rho}$, equation (12) becomes $\|\hat{\rho}\|^2 = -b(\hat{\boldsymbol{u}}, \hat{\rho}) = (\nabla \cdot \hat{\boldsymbol{u}}, \hat{\rho}) = \langle \boldsymbol{u}_D \cdot \boldsymbol{n}^\Omega, \hat{\rho}\rangle = 0$, implying $\hat{\rho} = 0$. Finally, the difference of equations (7) and (11) reduces to $\langle \lambda - \hat{\lambda}^t, \boldsymbol{v}\rangle_{\partial\mathcal{T}} = \langle \lambda^t - \hat{\lambda}^t, \boldsymbol{v}\rangle_{\partial\mathcal{T}} = 0$, for arbitrary test functions $\boldsymbol{v} \in \boldsymbol{X}$, and we conclude that $\hat{\lambda}^t = \lambda^t$. □

Remark 1. In the above proof we used the property stating that if $\langle \lambda^t, \boldsymbol{v}\rangle_{\partial\mathcal{T}} = 0$, for arbitrary $\boldsymbol{v} \in \boldsymbol{X}$, then $\lambda^t = 0$ must hold. That is, $\langle \lambda^t, \boldsymbol{v}\rangle_{\partial\mathcal{T}}$ defines an injective linear operator in $\boldsymbol{X}$ for any $\lambda^t \in \mathbf{\Lambda}^t$.

3 | SEMI-HYBRID-MIXED FINITE ELEMENT METHOD

The purpose is to construct discrete versions for the semi-hybrid-mixed formulation (11)-(14) using FE space settings $\mathcal{S}_h = \boldsymbol{X}_h \times \Psi_h \times \mathbf{\Lambda}^t_h \subset \mathcal{S}$, indexed by the characteristic mesh width h of the associated partitions $\mathcal{T}_h$ (and of the mesh skeleton Γ_h), which are assumed to be shape-regular, with shape-regularity factors independent of h.

HM-H(div)($\mathcal{S}_h$): find $(\boldsymbol{u}_h, p_h, \boldsymbol{\lambda}_h^t, \rho) \in \mathcal{S}_h \times \mathbb{R}$ such that

$$a_{\mathcal{T}_h}(\boldsymbol{u}_h, \boldsymbol{v}) - b(\boldsymbol{v}, p_h) + \langle \boldsymbol{\lambda}_h^t, \boldsymbol{v} \rangle_{\partial\mathcal{T}_h} = (\boldsymbol{f}, \boldsymbol{v}_h), \quad \forall \boldsymbol{v} \in \boldsymbol{X}_h, \tag{15}$$

$$b(\boldsymbol{u}_h, q) + (\rho, q) = 0, \quad \forall q \in \Psi_h, \tag{16}$$

$$\langle \boldsymbol{\eta}^t, \boldsymbol{u}_h \rangle_{\partial\mathcal{T}_h} = \langle \boldsymbol{\eta}^t, \boldsymbol{u}_D \rangle, \quad \forall \boldsymbol{\eta}^t \in \boldsymbol{\Lambda}_h^t, \tag{17}$$

$$(\xi, p_h) = 0, \quad \forall \xi \in \mathbb{R}. \tag{18}$$

Remark 2. As for the original weak formulation (7)-(10), equation (18) is a constraint enforcing that p_h has zero mean over Ω. In principle, we could formulate HM-H(div)($\mathcal{S}_h$) without the Lagrange multiplier ρ, searching p_h directly in $\Psi_{0h} = \Psi_h \cap L_0^2(\Omega)$. In fact, equation (16) implies $\rho = 0$, for taking constant $q = \rho$ we obtain $\|\rho\|_{L^2}^2 = -b(\boldsymbol{u}_h, \rho) = -\langle \boldsymbol{u}_D \cdot \boldsymbol{n}, \rho \rangle = 0$. In practice, the introduction of ρ is for sake of simplifying coding, to avoid the construction of pressure shape functions with vanishing mean. Consequently, equation (16) exactly ensures the divergence-free property for the velocity approximation $\boldsymbol{u}_h$.

Even though the original formulation (11)-(14) is well posed, this may not be true for the HM-H(div)($\mathcal{S}_h$) formulation. In fact, the FE spaces of each field cannot be chosen independently one from the other: there must be compatibility relations between them. Following Brezzi's theory, as applied in [31,32,2] for similar contexts, let us introduce the following subspaces associated to the pairs $\{\boldsymbol{X}_h, \Psi_h\}$ and $\{\boldsymbol{X}_h, \boldsymbol{\Lambda}_h^t\}$:

$$\boldsymbol{Z}_h(0) = \{\boldsymbol{v} \in \boldsymbol{X}_h; b(\boldsymbol{v}, q) = 0, \forall q \in \Psi_h\},$$
$$\boldsymbol{X}_h(\boldsymbol{u}_D) = \{\boldsymbol{v} \in \boldsymbol{X}_h;\ \langle \boldsymbol{\eta}^t, \boldsymbol{v} \rangle_{\partial\mathcal{T}_h} = \langle \boldsymbol{\eta}^t, \boldsymbol{u}_D \rangle,\ \forall \boldsymbol{\eta}^t \in \boldsymbol{\Lambda}_h^t\}.$$

It is clear from (16) and (17) that $\boldsymbol{u}_h \in \boldsymbol{X}_h(\boldsymbol{u}_D) \cap \boldsymbol{Z}_h(0)$.

According to Brezzi's theory, the HM-H(div)($\mathcal{S}_h$) formulation is well posed provided the following conditions are satisfied:

(S1) $\inf a_{\mathcal{T}_h}(\boldsymbol{v}, \boldsymbol{v})^{1/2} > 0$ whenever $\boldsymbol{v} \in \boldsymbol{Z}_h(0) \cap \boldsymbol{X}_h(0)$, $\|\boldsymbol{v}\|_{1,\mathcal{T}_h} = 1$.

(S2) There exists a positive constant C, such that

$$\sup_{\boldsymbol{v} \in \boldsymbol{X}_h} \left[b(\boldsymbol{v}, q) + \langle \boldsymbol{\eta}^t, \boldsymbol{v} \rangle_{\partial\mathcal{T}_h} \right] \geq C \|\boldsymbol{v}\|_{1,\mathcal{T}_h} (\|q\|_{L^2(\Omega)} + \|\boldsymbol{\eta}^t\|_{\boldsymbol{\Lambda}}). \tag{19}$$

for arbitrary $q \in \Psi_h$ and $\boldsymbol{\eta}^t \in \boldsymbol{\Lambda}_h^t$, independently of the discretization parameters.

As aforementioned, $\|\boldsymbol{v}\|_{a_{\mathcal{T}_h}} = (\boldsymbol{v}, \boldsymbol{v})^{1/2}$ defines a norm in $\boldsymbol{X}$, so that (S1) holds for all $\boldsymbol{v} \in \boldsymbol{X}_h \subset \boldsymbol{X}$. Concerning (S2), condition (19) is known to be valid in the absence of the tangential trace variable. Namely, for a given divergence-consistency FE pair $\boldsymbol{X}_h \times \Psi_h$, such that

$$\nabla \cdot \boldsymbol{X}_h \subseteqq \Psi_h, \tag{20}$$

which is used for velocity and pressure approximations in Darcy mixed formulations, an inf-sup condition

$$\inf_{q \in \Psi_h} \sup_{\boldsymbol{v} \in \boldsymbol{X}_h} b(\boldsymbol{v}, q) \geq C_1 \|\boldsymbol{v}\|_{1,\mathcal{T}_h} \|q\|_{L^2(\Omega)} \tag{21}$$

holds with $C_1 > 0$ independently of the discretization parameters.

However, as it will become clear in the following sections, in order to obtain a constant $C_2 > 0$ such that

$$\inf_{\boldsymbol{\eta}^t \in \boldsymbol{\Lambda}_h^t,} \sup_{\boldsymbol{v} \in \boldsymbol{Z}_h(0),} \langle \boldsymbol{\eta}^t, \boldsymbol{v} \rangle_{\partial\mathcal{T}_h} \geq C_2 \|\boldsymbol{v}\|_{1,\mathcal{T}_h} \|\boldsymbol{\eta}^t\|_{\boldsymbol{\Lambda}}, \tag{22}$$

the choice of $\boldsymbol{\Lambda}_h^t \subset \boldsymbol{\Lambda}^t$ is a more subtle task (even for solvability purposes, when C_2 is allowed to change with the discretization parameters of $\mathcal{S}_h$).

3.1 | Solvability

Theorem 3. In addition to the divergence-consistency property (20), suppose $\mathcal{S}_h$ is a given FE space configuration verifying the trace compatibility condition (22). Then the associated HM-H(div)($\mathcal{S}_h$) formulation has a unique solution.

Proof. We have to evaluate the homogeneous version of system (15)-(18) by taking $\boldsymbol{f} = 0$ and $\boldsymbol{u}_D = 0$. Firstly, consider $(\boldsymbol{u}_h, \lambda_h^t) \in \mathbf{Z}_h(0) \times \boldsymbol{\Lambda}_h^t$ solving the homogeneous system

$$a_{\mathcal{T}_h}(\boldsymbol{u}_h, \boldsymbol{v}) + \langle \lambda_h^t, \boldsymbol{v} \rangle_{\partial \mathcal{T}_h} = 0, \quad \forall \boldsymbol{v} \in \mathbf{Z}_h(0), \tag{23}$$

$$\langle \boldsymbol{\eta}^t, \boldsymbol{u}_h \rangle_{\partial \mathcal{T}_h} = 0, \quad \forall \boldsymbol{\eta}^t \in \boldsymbol{\Lambda}_h^t. \tag{24}$$

By inserting $\boldsymbol{v} = \boldsymbol{u}_h$ as test function in the first equation (23) and using the second equation (24), we obtain $a_{\mathcal{T}_h}(\boldsymbol{u}_h, \boldsymbol{u}_h) = 0$. Recalling the ellipticity property (S1), we conclude that $\boldsymbol{u}_h = 0$. Consequently, equation (23) reduces to $\langle \lambda_h^t, \boldsymbol{v} \rangle_{\partial \mathcal{T}_h} = 0, \forall \boldsymbol{v} \in \mathbf{Z}_h(0)$, implying $\lambda_h^t = 0$ as a consequence of the trace compatibility condition (22). Finally, the homogeneous version of equation (15) becomes $b(\boldsymbol{v}, p_h) = 0, \ \forall \boldsymbol{v} \in \boldsymbol{X}_h$, and the divergence-consistency property (20) implies that $p_h = 0$. □

Remark 3. Following Remark 10.3 in [32], let us consider shape functions $\{\boldsymbol{v}_j\}$ of $\boldsymbol{Z}_h(0)$ and $\{\boldsymbol{\eta}_\ell^t\}$ of $\boldsymbol{\Lambda}_h^t$ and set $\mathbf{C}^T = [\langle \boldsymbol{\eta}_\ell^t, \boldsymbol{v}_j \rangle_{\partial \mathcal{T}_h}]$. The trace compatibility condition implies that $\mathbf{C}^T$ defines an injective mapping. This property may also be interpreted as expressing the fact $\mathbf{C}^T$ has rank equal to dimension of $\boldsymbol{\Lambda}_h^t$, from where the term rank condition comes from, according to [33].

Remark 4. Following the algebraic aspects of saddle point problems in Chapter 3 of [4], it is known that, despite of being a fundamental condition, solvability is not sufficient to provide a good method, and stability is actually needed. This is a concept that applies to a sequence of discretized problems, for which the solvability hypotheses are required to be valid independently of the discretization parameters. The hybridization of a class of stable nonconforming methods proposed in the literature shall be discussed in Section 4.2, revealing that stability of the tangent trace approximation can be obtained by carefully increasing the internal polynomial order of velocity approximation.

3.2 | Nonconforming Strang-type error estimates

A starting point to obtain a priori error estimations for nonconforming methods could be inspired by the classic Strang's Second Lemma, where enters into play not only the best approximation error of the exact solution, but also the so called consistency error (measuring the nonconformity of the approximate solution). For instance, this approach was followed for nonconforming mixed methods for Stokes problems in [5,34]. In a similar way, error estimates were obtained for nonconforming formulations in [15,16,17] for Stokes-Brinkman problems using $H(\mathrm{div})$-conforming velocity approximations (see Section 4.2). In the sequence, we present a similar error analysis for the semi-hybrid-mixed HM-H(div)($\mathcal{S}_h$) methods.

Theorem 4. Let $(\boldsymbol{u}, p, \lambda^t, 0) \in \mathcal{S} \times \mathbb{R}$ be the exact solution of formulation (11)-(14), and suppose the FE setting $\mathcal{S}_h^{\mathrm{div}} = \boldsymbol{X}_h \times \Psi_h \times \boldsymbol{\Lambda}_h^t$ is well posed. If $(\boldsymbol{u}_h, p_h, \lambda_h^t, 0) \in \mathcal{S}_h \times \mathbb{R}$ solves the HM-H(div)($\mathcal{S}_h$) system (15)-(18), then

$$\|\boldsymbol{u} - \boldsymbol{u}_h\|_{a_{\mathcal{T}_h}} \lesssim \left[\inf_{\boldsymbol{z} \in \boldsymbol{Z}_h(0)} \|\boldsymbol{u} - \boldsymbol{z}\|_{a_{\mathcal{T}_h}} + \sup_{\boldsymbol{v} \in \boldsymbol{Z}_h(0) \setminus \{0\}} \frac{\langle \lambda_h^t - \lambda^t, \boldsymbol{v} \rangle_{\partial \mathcal{T}_h}}{\|\boldsymbol{v}\|_{a_{\mathcal{T}_h}}} \right], \tag{25}$$

$$\|\lambda^t - \lambda_h^t\|_{\boldsymbol{\Lambda}} \lesssim M^{1/2} \|\boldsymbol{u} - \boldsymbol{u}_h\|_{a_{\mathcal{T}_h}}, \tag{26}$$

$$\|p - p_h\|_{L^2} \lesssim \left[\|p - \Pi_h^p p\|_{L^2} + M^{1/2} \|\boldsymbol{u} - \boldsymbol{u}_h\|_{a_{\mathcal{T}_h}} + \|\lambda^t - \lambda_h^t\|_{\boldsymbol{\Lambda}} \right], \tag{27}$$

where $\Pi_h^p \, p \in \Psi_{0h}$ defines the L^2-projection of $p \in \Psi_0$ onto Ψ_{0h} and $M = \max\{\mu, \alpha\}$.

Proof. We already know that $\boldsymbol{u} \in H^1(\Omega)$, $\nabla \cdot \boldsymbol{u} = 0$, $\boldsymbol{u}|_{\partial\Omega} = \boldsymbol{u}_D$, and $p \in \Psi_0$. In the discrete context, $\boldsymbol{u}_h \in \boldsymbol{X}_h(\boldsymbol{u}_D) \cap \boldsymbol{Z}_h(0)$ and $p_h \in \Psi_{0h}$. Consider the errors $\boldsymbol{u} - \boldsymbol{u}_h$, $p - p_h$ and $\lambda^t - \lambda_h^t$. Then

$$a_{\mathcal{T}_h}(\boldsymbol{u} - \boldsymbol{u}_h, \boldsymbol{v}) - b(\boldsymbol{v}, p - p_h) + \langle \lambda^t - \lambda_h^t, \boldsymbol{v} \rangle_{\partial \mathcal{T}_h} = 0, \quad \forall \boldsymbol{v} \in \boldsymbol{X}_h, \tag{28}$$

$$b(\boldsymbol{u} - \boldsymbol{u}_h, q) = 0, \quad \forall q \in \Psi_{0h}. \tag{29}$$

For an arbitrary $\boldsymbol{z} \in \boldsymbol{Z}_h(0)$, set $\boldsymbol{v} = \boldsymbol{z} - \boldsymbol{u}_h \in \boldsymbol{Z}_h(0)$ as test function in (28) to obtain

$$a_{\mathcal{T}_h}(\boldsymbol{u} - \boldsymbol{u}_h, \boldsymbol{v}) + \langle \lambda^t - \lambda_h^t, \boldsymbol{v} \rangle_{\partial \mathcal{T}_h} = 0, \tag{30}$$

which can be expressed as $a_{\mathcal{T}_h}(\boldsymbol{z} - \boldsymbol{u}, \boldsymbol{v}) + \langle \lambda_h^t - \lambda^t, \boldsymbol{v} \rangle_{\partial \mathcal{T}} = a_{\mathcal{T}_h}(\boldsymbol{v}, \boldsymbol{v}) = \|\boldsymbol{v}\|_{a_{\mathcal{T}_h}}^2$. Thus, for $\boldsymbol{v} \neq 0$ we obtain

$$\|\boldsymbol{v}\|_{a_{\mathcal{T}_h}} \leq \|a_{\mathcal{T}_h}\| \|\boldsymbol{z} - \boldsymbol{u}\|_{a_{\mathcal{T}_h}} + \frac{\langle \lambda_h^t - \lambda^t, \boldsymbol{v}_h \rangle_{\partial \mathcal{T}_h}}{\|\boldsymbol{v}\|_{a_{\mathcal{T}_h}}},$$

and estimate (25) follows by using the triangle inequality $\|\boldsymbol{u}-\boldsymbol{u}_h\|_{a_{\mathcal{T}_h}} \leq \|\boldsymbol{u}-\boldsymbol{z}\|_{a_{\mathcal{T}_h}} + \|\boldsymbol{z}-\boldsymbol{u}_h\|_{a_{\mathcal{T}_h}} = \|\boldsymbol{u}-\boldsymbol{z}\|_{a_{\mathcal{T}_h}} + \|\boldsymbol{v}\|_{a_{\mathcal{T}_h}}$. Moreover, using the equation (30) and the inf-sup condition (22) we obtain

$$\|\boldsymbol{v}\|_{1,\mathcal{T}_h}\|\lambda^t-\lambda_h^t\|_{\boldsymbol{\Lambda}} \lesssim \langle\lambda^t-\lambda_h^t,\boldsymbol{v}\rangle_{\partial\mathcal{T}_h} = a_{\mathcal{T}_h}(\boldsymbol{u}_h-\boldsymbol{u},\boldsymbol{v}) \leq \|a_{\mathcal{T}_h}\|\|\boldsymbol{u}-\boldsymbol{u}_h\|_{a_{\mathcal{T}_h}}\|\boldsymbol{v}\|_{a_{\mathcal{T}_h}},$$

which implies the tangential trace error estimate (27) after using the property $\|\boldsymbol{v}\|_{a_{\mathcal{T}_h}} \leq M^{1/2}\|\boldsymbol{v}\|_{1,h}$.

Finally, using the property $b(\boldsymbol{v}, p-\Pi_h^p p) = 0$ for arbitrary $\boldsymbol{v} \neq 0 \in \boldsymbol{X}_h$, implied by (20), the inf-sup condition (21), and equations (28)-(29), we obtain

$$\begin{aligned}\|\boldsymbol{v}\|_{1,\mathcal{T}_h}\|\Pi_h^p p-p_h\|_{L^2} \lesssim b(\boldsymbol{v},\Pi_h^p p-p_h) = b(\boldsymbol{v},p-p_h) &= a_{\mathcal{T}_h}(\boldsymbol{u}-\boldsymbol{u}_h,\boldsymbol{v}) + \langle\lambda^t-\lambda_h^t,\boldsymbol{v}\rangle_{\partial\mathcal{T}_h}\\ &\leq \|a_{\mathcal{T}_h}\|\|\boldsymbol{u}-\boldsymbol{u}_h\|_{a_{\mathcal{T}_h}}\|\boldsymbol{v}\|_{a_{\mathcal{T}_h}} + \langle\lambda^t-\lambda_h^t,\boldsymbol{v}\rangle_{\partial\mathcal{T}_h}.\end{aligned}$$

As a consequence of the above inequality and the triangle inequality $\|p-p_h\|_{L^2} \leq \|p-\Pi_h^p\|_{L^2} + \|\Pi_h^p-p_h\|_{L^2}$, the estimate (27) holds. □

To make Theorem 4 effective, the terms on the right hand sides of the error inequalities need to be elaborated in order to obtain convergent rates of the variables involved:

(i) The best approximation error in the first term on the right-hand side of (25) measures how well the exact velocity $\boldsymbol{u} \in \boldsymbol{Z}(0)$ can be approximated by nonconforming functions in $\boldsymbol{Z}_h(0)$. Typically, this term can be estimated by the interpolant error $\|\boldsymbol{u}-\Pi_h^u\boldsymbol{u}\|_{a_{\mathcal{T}_h}}$ of the exact velocity field $\boldsymbol{u}$ given by an operator $\Pi_h : H^1(\Omega,\mathbb{R}^d) \to \boldsymbol{X}_h$ commuting the divergence $\nabla\cdot\Pi_h^u\boldsymbol{u} = \Pi_h^\beta\nabla\cdot\boldsymbol{u}$.

(ii) The second term in (25) measures the nonconformity of $\boldsymbol{u}_h$, which would be zero for H^1-conforming velocity approximations. It is also known as consistency error in the context of nonconforming methods. A poor choice of the Lagrange multiplier space, which is constrained by the trace compatibility condition to ensure solvability, may reduce the velocity convergence rate under the optimal approximation order in the first term.

(iii) The first term on the right-hand side of (27) is the optimal L^2-error approximation of the pressure p, which may also be dominated by the second and third terms.

In the next section, the trace compatibility constraint (22) shall be numerically verified for some classic divergence-consistent FE pairs $\boldsymbol{X}_h \times \Psi_h$. Numerical L^2-errors are shown for them in Section 6, where convergence is verified against exact solutions, approximations by well-established DG formulations, and other numerical or experimental results found in the literature. The applicability of the above theoretical error analysis for these numerical verifications is still limited, for velocity error estimations in L^2-norms are still missing.

4 | EXAMPLES OF HM-H(div)(S_H) FORMULATIONS

The discussion of the previous section reveals that for the solvability of the HM-H(div)(S_h) formulation the FE space setting $S_h = \boldsymbol{X}_h \times \Psi_h \times \boldsymbol{\Lambda}_h^t$ is required to verify the following compatibility conditions:

1. The pair $\{\boldsymbol{X}_h, \Psi_h\}$ is divergence-compatible according to (20). This is the property required for FE pairs applied for Darcy flow simulations.

2. The pair $\{\boldsymbol{X}_h, \boldsymbol{\Lambda}_h^t\}$ is trace compatible according to (22).
The verification of trace compatibility conditions occurring in hybrid methods is usually a rather technical issue, requiring an extra effort, as revealed in the analysis of the early primal hybrid method for Poisson problems considered in [31].

Our purpose here is to discuss solvability aspects for some examples where $\boldsymbol{X}_h \times \Psi_h$ are classic divergence-compatible FE pairs $\{\boldsymbol{X}_h, \Psi_h\}$ based on partitions $\mathcal{T}_h$ whose elements K are geometrically mapped from a reference element $\hat{K}$ of one of the usual geometry:

- For triangular elements K: $\hat{T} = \{(\hat{x},\hat{y});\ \hat{x}\geq 0, \hat{y}\geq 0, \hat{x}+\hat{y}\leq 1\}$.
- For quadrilateral elements K: $\hat{R} = [-1,1]\times[-1,1]$.

- For tetrahedra K: $\hat{T}e = \{(\hat{x}, \hat{y}, \hat{z});\ \hat{x} \geq 0, \hat{y} \geq 0, \hat{z} \geq 0, \hat{x} + \hat{y} + \hat{z} \leq 1\}$.
- For hexahedra K: $\hat{H} = [-1, 1] \times [-1, 1] \times [-1, 1]$.

Approximation spaces $\boldsymbol{X}(\hat{K})$ and $\Psi(\hat{K})$ defined in the reference element are supposed to be divergence-compatible polynomial spaces, such that $\nabla \cdot \boldsymbol{X}(\hat{K}) = \Psi(\hat{K})$. Moreover, the direct sum decomposition $\boldsymbol{X}(\hat{K}) = \boldsymbol{X}^{\partial}(\hat{K}) \oplus \mathring{\boldsymbol{X}}(\hat{K})$ is considered in terms of internal velocity fields $\mathring{\boldsymbol{X}}(\hat{K})$, with vanishing normal components over $\partial\hat{K}$, and the external velocities $\boldsymbol{X}^{\partial}(\hat{K})$ otherwise. Given the geometric invertible map $F_K : \hat{K} \to K$, the FE pair $\boldsymbol{X}(\hat{K}) \times \Psi(\hat{K})$ is mapped to K to form FE spaces $\boldsymbol{X}(K) \times \Psi(K)$ by the following pullback operators:

- Scalar FE functions $p \in \Psi(K)$: $p = \mathcal{F}(\hat{p}) := \hat{p} \circ F_K^{-1}$, $\hat{p} \in \Psi(\hat{K})$. Recall that, $\mathcal{F}$ is an isomorphism from $L^2(\hat{K})$ onto $L^2(K)$ (and also from $H^1(\hat{K})$ onto $H^1(K)$).
- Vector FE functions $\boldsymbol{v} \in \boldsymbol{X}(K) \subset H(\mathrm{div}, K)$: $\boldsymbol{v} = \mathcal{G}_K(\hat{\boldsymbol{v}}) := \left[\frac{1}{\mathbf{J}_K} DF_K \hat{\boldsymbol{v}}\right] \circ F_K^{-1}$, $\hat{\boldsymbol{v}} \in \boldsymbol{X}(\hat{K})$, where DF_K is the Jacobian matrix of F_K, and $\mathbf{J}_K = \left|\det(DF_K)\right|$ (constant for affine elements).

The mapping $\mathcal{G}_K$, known as Piola transformation, is an isomorphism from $H(\mathrm{div}; \hat{\mathrm{K}})$ onto $H(\mathrm{div}; \mathrm{K})$, verifying $\nabla \cdot \mathcal{G}_K(\hat{\boldsymbol{v}}) = \mathcal{F}_K\left[\frac{1}{\mathbf{J}_K} \hat{\nabla} \cdot \hat{\mathbf{v}}\right]$, so that $(\nabla \cdot \mathcal{G}_K(\hat{\boldsymbol{v}}), \mathcal{F}(\hat{p}))_K = (\nabla \cdot \hat{\boldsymbol{v}}, \hat{p})_{\hat{K}}$, and $\langle \mathcal{G}_K(\hat{\boldsymbol{v}}) \cdot \boldsymbol{n}^K, \mathcal{F}(\hat{p})\rangle_{\partial K} = \langle \hat{\boldsymbol{v}} \cdot \boldsymbol{n}^{\hat{K}}, \hat{p}\rangle_{\partial \hat{K}}$. Accordingly, the action of $\mathcal{G}_K$ preserves the divergence-consistency property $\nabla \cdot \boldsymbol{X}(K) = \Psi(K)$ and the direct sum decomposition $\boldsymbol{X}(K) = \boldsymbol{X}^{\partial}(K) \oplus \mathring{\boldsymbol{X}}(K)$.

Let Γ_h be the skeleton mesh formed by the facets $E \subset \partial K$ (faces in 3D elements or edges in 2D cases). Similarly, given geometric invertible maps $F_E : \hat{F} \to E$ and vector trace spaces $\boldsymbol{W}^t(\hat{E})$, vector trace FE spaces $\boldsymbol{W}^t(E)$ are defined in E by the pullback operator:

- Vector FE functions $\boldsymbol{\eta}^t \in \boldsymbol{W}^t(E)$, $E \in \Gamma_h$: $\boldsymbol{\eta}^t = \mathcal{G}_E(\hat{\boldsymbol{\eta}}^t) := \left[\frac{1}{\mathbf{J}_E} DF_E \hat{\boldsymbol{\eta}}^t\right] \circ F_E^{-1}$, $\hat{\boldsymbol{\eta}}^t \in \boldsymbol{W}^t(\hat{E})$.

Finally, finite dimensional FE approximation spaces $\boldsymbol{X}_h \subset \boldsymbol{X}$, $\Psi_h \subset \Psi$ are piecewise defined over $\mathcal{T}_h$ by the usual assembly process of the local spaces $\boldsymbol{X}(K), \Psi(K)$. Similarly, $\boldsymbol{\Lambda}_h^t \subset \boldsymbol{\Lambda}^t$ is piecewise defined over Γ_h as $\boldsymbol{\Lambda}_h^t = \{\boldsymbol{\eta}^t \in \boldsymbol{\Lambda}^t; \boldsymbol{\eta}^t|_E \in \boldsymbol{W}^t(E),\ E \in \Gamma_h\}$.

Some classic examples of divergence-compatible FE pairs $\boldsymbol{X}(\hat{K}) \times \Psi(\hat{K})$ are displayed in Table 1 for reference elements of triangular ($\hat{T}$), quadrilateral ($\hat{R}$), tetrahedral ($\hat{T}e$) or hexahedral ($\hat{H}$) geometry. The following polynomial spaces are used in $\hat{K}$: scalar polynomials $\mathbb{P}_k(\hat{K})$ of total degree at most k, $\tilde{\mathbb{P}}_k(\hat{K})$ denoting the homogeneous ones; vector versions $\mathbb{P}_k(\hat{K}, \mathbb{R}^d)$ are also used; the polynomials in $\mathbb{Q}_{k,m}(\hat{K})$ or $\mathbb{Q}_{k,m,n}(\hat{K})$ have maximum degree k, m or n in each coordinate.

Table 1 Examples of FE pairs $\tilde{X}(\hat{K}) \times \Psi(\hat{K})$ in the reference element for velocity and pressure fields

$\hat{K}$	Method	$\mathbf{X}(\hat{K})$	$\Psi(\hat{K})$
$\hat{T}$	$BDM(k)$[35]	$\mathbb{P}_k(\hat{K}, \mathbb{R}^2)$	$\mathbb{P}_{k-1}(\hat{K})$
	$RT(k)$[36]	$\mathbb{P}_k(\hat{K}, \mathbb{R}^2) \oplus \mathbf{x}\tilde{\mathbb{P}}_k(\hat{K})$	$\mathbb{P}_k(\hat{K})$
	$BDM^+(k)$[37]	$\mathbb{P}_k^{\partial}(\hat{K}, \mathbb{R}^2) \oplus \mathring{\mathbb{P}}_{k+1}(\hat{K}, \mathbb{R}^2)$	$\mathbb{P}_k(\hat{K})$
$\hat{R}$	$RT(k)$[36]	$\mathbb{Q}_{k+1,k} \times \mathbb{Q}_{k,k+1}(\hat{K})$	$\mathbb{Q}_{k,k}(\hat{K})$
	$RT^+(k)$[38]	$\boldsymbol{X}^{\partial}_{RT(k)}(\hat{K}) \oplus \mathring{\boldsymbol{X}}_{RT(k+1)}(\hat{K})$	$\mathbb{Q}_{k+1,k+1}(\hat{K})$
$\hat{T}e$	$BDM(k)$[39]	$\mathbb{P}_k(\hat{K}, \mathbb{R}^3)$	$\mathbb{P}_{k-1}(\hat{K})$
	$RT(k)$[40]	$\mathbb{P}_k(\hat{K}, \mathbb{R}^3) \oplus \mathbf{x}\tilde{\mathbb{P}}_k(\hat{K})$	$\mathbb{P}_k(\hat{K})$
	$BDM^+(k)$[37]	$\mathbb{P}_k^{\partial}(\hat{K}, \mathbb{R}^3) \oplus \mathring{\mathbb{P}}_{k+1}(\hat{K}, \mathbb{R}^3)$	$\mathbb{P}_k(\hat{K})$
$\hat{H}$	$RT(k)$[40]	$\mathbb{Q}_{k+1,k,k} \times \mathbb{Q}_{k,k+1,k} \times \mathbb{Q}_{k,k,k+1}(\hat{K})$	$\mathbb{Q}_{k,k,k}(\hat{K})$
	$RT^+(k)$[41]	$\boldsymbol{X}^{\partial}_{RT(k)}(\hat{K}) \oplus \mathring{\boldsymbol{X}}_{RT(k+1)}(\hat{K})$	$\mathbb{Q}_{k+1,k+1,k+1}(\hat{K})$

To be combined with $\tilde{X}(\hat{K}) \times \Psi(\hat{K})$, let us consider Lagrange multiplier vector polynomial spaces of the following types:

- For edges: $\boldsymbol{W}^t(\hat{E}) = \mathbb{P}_m(\hat{E})\boldsymbol{\tau}^{\hat{E}}$ on edges $\hat{E}$;
- For triangular facets: $\boldsymbol{W}^t(\hat{E}) = \hat{\boldsymbol{n}} \wedge \mathbb{P}_m(\hat{E}, \mathbb{R}^3)$;

- For quadrilateral facets: $\boldsymbol{W}^t(\hat{E}) = \hat{\boldsymbol{n}} \wedge \mathbb{Q}_{m,m}(\hat{E}, \mathbb{R}^3)$.

The parameter m has to be be chosen properly for the verification of the trace compatibility property (22). In the sequence we discuss a numerical test for the verification of the trace compatibility condition for the FE spaces based on triangular an quadrilateral elements.

4.1 | Verification of the trace compatibility condition (22)

The purpose is to verify in which extent the divergence-free subspaces $\boldsymbol{Z}_h(0) \subset \boldsymbol{X}_h$ associated to some examples shown in Table 1 are rich enough to enforce a trace compatibility condition (22) with respect to the Lagrange multiplier space $\boldsymbol{\Lambda}_h^t$, by properly choosing the polynomial degree m. As observed in Remark 3 after the proof of Theorem 3, for shape functions $\{\boldsymbol{\eta}_\ell^t\}$ of $\boldsymbol{\Lambda}_h^t$ and $\{\boldsymbol{v}_j\}$ of $\boldsymbol{Z}_h(0)$, the matrix $\mathbf{C}^T = [\langle \boldsymbol{\eta}_\ell^t, \boldsymbol{v}_j \rangle_{\partial \mathcal{T}_h}]$ is required to be injective, which can be expresses by the rank condition $\operatorname{rank} \mathbf{C}^T = \dim \boldsymbol{\Lambda}_h^t$. For that, we propose a numerical test of rank condition verification for regions $\Omega = K_0 \cup K_1$, the elements in $\mathcal{T}_h = \{K_0, K_1\}$ being triangles or rectangles, as represented in Figure 1. In each case, the characterization of $\boldsymbol{Z}_h(0)$ is

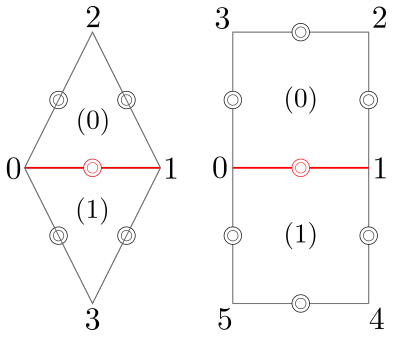

Figure 1 Triangular and rectangular partitions $\mathcal{T}_h = \{K_0, K_1\}$ used for the rank condition numerical tests.

Table 2 Exact FE sequences for $BDM(k)$ in $\hat{T}$, $RT(k)$ in $\hat{R}$, and for their enriched versions $BDM^+(k)$ and $RT^+(k)$, respectively.

Space	$BDM(k)$	$BDM^+(k)$
$U(\hat{T}) \subset H^1(\hat{T})$	$\mathbb{P}_{k+1}(\hat{T})$	$\mathbb{P}^\partial_{k+1}(\hat{T}) \oplus \mathring{\mathbb{P}}_{k+2}(\hat{T})$
$\downarrow \nabla\times$	$\downarrow \nabla\times$	$\downarrow \nabla\times$
$\boldsymbol{X}(\hat{T}) \subset \mathbf{H}(\mathrm{div}, \hat{T})$	$\mathbb{P}_k(\hat{T}, \mathbb{R}^2)$	$\mathbb{P}^\partial_k(\hat{T}, \mathbb{R}^2) \oplus \mathring{\mathbb{P}}_{k+1}(\hat{T}, \mathbb{R}^2)$
$\downarrow \nabla\cdot$	$\downarrow \nabla\cdot$	$\downarrow \nabla\cdot$
$\Psi(\hat{T}) \subset L^2(\hat{T})$	$\mathbb{P}_{k-1}(\hat{T})$	$\mathbb{P}_k(\hat{T})$

Space	$RT(k)$	$RT^+(k)$
$U(\hat{R}) \subset H^1(\hat{R})$	$\mathbb{Q}_{k+1,k+1}(\hat{R})$	$\mathbb{Q}^\partial_{k+1,k+1}(\hat{R}) \oplus \mathring{\mathbb{Q}}_{k+2,k+2}(\hat{R})$
$\downarrow \nabla\times$	$\downarrow \nabla\times$	$\downarrow \nabla\times$
$\boldsymbol{X}(\hat{R}) \subset \mathbf{H}(\mathrm{div}, \hat{R})$	$\boldsymbol{X}_{RT(k)}(\hat{R})$	$\boldsymbol{X}^\partial_{RT(k)}(\hat{R}) \oplus \mathring{\boldsymbol{X}}_{RT(k+1)}(\hat{R})$
$\downarrow \nabla\cdot$	$\downarrow \nabla\cdot$	$\downarrow \nabla\cdot$
$\Psi(\hat{R}) \subset L^2(\hat{R})$	$\mathbb{Q}_{k,k}(\hat{R})$	$\mathbb{Q}_{k+1,k+1}(\hat{R})$

crucial, which can be obtained in the context of the exact FE sequences shown in Table 2, where for scalar functions $\nabla \times \varphi =$

$[\partial\varphi/\partial y, -\partial\varphi/\partial x]^T$. They are discrete versions of the exact differential sequence $H^1(\hat{K}) \xrightarrow{\nabla\times} \mathbf{H}(\mathrm{div}, \hat{K}) \xrightarrow{\nabla\cdot} L^2(\hat{K})$, meaning that each space is mapped into the succeeding space by the given differential operator, the composition of two consecutive maps being zero. In such context, if the subspace $U(\hat{K}) \subset H^1(\hat{K})$ combines with the space $\boldsymbol{X}(\hat{K}) \subset \mathbf{H}(\mathrm{div}, \hat{K})$, then the corresponding divergence-free functions are in $\nabla \times U(\hat{K}) \subset \boldsymbol{X}(\hat{K})$. Thus, the cardinality of a given basis $\mathcal{B}_h^{\mathrm{grad}}$ of U_h is one unit more than the dimension of $\boldsymbol{Z}_h(0)$. Under this point of view, we define shape functions $\mathcal{B}_h^{\mathrm{grad,filt}}$ by removing one arbitrary vertex function from a basis $\mathcal{B}_h^{\mathrm{grad}}$ for U_h and set $\mathcal{B}_h^{\mathrm{div},0} = \nabla \times \mathcal{B}_h^{\mathrm{grad,filt}}$ for a basis for $\boldsymbol{Z}_h(0)$.

Taking the tangential traction spaces $\boldsymbol{\Lambda}_\gamma^t$ with $m = k - 1$, the rank of $\mathbf{C}^T$ and the dimension of $\boldsymbol{\Lambda}_h^t$ are presented in Table 3. Comparing the results, trace compatibility (22) is confirmed for $RT(k)$, $RT^+(k)$ and $BDM^+(k)$ cases. However, it is not verified for $BDM(k)$.

Table 3 Rank condition tests

k	Rank of $\mathbf{C}^T$		$\dim \boldsymbol{\Lambda}_h^t$	k	Rank of $\mathbf{C}^T$		$\dim \boldsymbol{\Lambda}_h^t$
	$BDM(k)$	$BDM^+(k)$			$RT(k)$	$RT^+(k)$	
1	4	5	5	1	7	7	7
2	9	10	10	2	14	14	14
3	14	15	15	3	21	21	21

4.2 | Hybridization of nonconforming methods

Another approach for the Stokes-Brinkman problem (1)-(3) based on divergence-compatible FE pairs $\boldsymbol{X}_h \times \Psi_h$ considers the nonconforming formulation (without hybridization).

Problem ($\mathrm{P_h}$): find $(\tilde{\boldsymbol{u}}_h, \tilde{p}_h) \in \boldsymbol{X}_h(\boldsymbol{u}_D) \times \Psi_{0h}$ such that

$$a_h(\tilde{\boldsymbol{u}}_h, \boldsymbol{v}) - b(\boldsymbol{v}, \tilde{p}_h) = (\boldsymbol{f}, \boldsymbol{v}_h), \quad \forall \boldsymbol{v} \in \boldsymbol{X}_h(0), \tag{31}$$

$$b(\tilde{\boldsymbol{u}}_h, q) = 0, \qquad \forall q \in \Psi_{0h}. \tag{32}$$

We already know that if $(\boldsymbol{u}_h, p_h, \boldsymbol{\lambda}^t, 0) \in \mathcal{S}_h \times \mathbb{R}$ solves of the HM-H(div)($\mathcal{S}_h$) formulation then $\boldsymbol{u}_h \in \boldsymbol{X}_h(\boldsymbol{u}_D)$ and $p_h \in \Psi_{0h}$. Moreover, by testing equation (15) with $\boldsymbol{v}_h \in \boldsymbol{X}_h(0)$ and equation (16) with $q_h \in \Psi_{0h}$, we conclude that $(\tilde{\boldsymbol{u}}_h, \tilde{p}_h) = (\boldsymbol{u}_h, p_h)$ solves Problem ($\mathrm{P_h}$). In this section we show that the converse is also true for solutions of some known well posed cases of Problem ($\mathrm{P_h}$).

Having in mind the construction of well posed FE settings $\boldsymbol{X}_h(\boldsymbol{u}_D) \times \Psi_{0h}$ for Problem ($\mathrm{P_h}$), some first order methods based on simplicial meshes (for triangles or tetrahedra) were derived in [14,42,16], and extended in [17] to higher order cases. First order examples for affine quadrilateral and hexaheral elements were proposed in [18,19]. In general terms, the approach of these methods is to combine the following tools:

1. There is a basic divergence-compatible FE pair $\boldsymbol{V}(K) \times \Psi(K)$. For simplicial elements, the examples in [42,16] are for the FE pair $BDM(1)$, and in [17] they are for $BDM(k)$ or $RT(k)$, $k \geq 1$. The cases in [18,19] are for the $BDM(1)$ elements in quadrilateral or hexaedral elements (see [4]). In all these cases, the velocity normal traces are of degree k.
2. There is a tangential FE trace space $\boldsymbol{W}^t(\partial K)$ defined by piecewise vector polynomials of degree $m = k - 1$.
3. A complementary divergence-free bubble polynomial space is constructed in the form $\boldsymbol{H}(K) = \mathrm{curl}\,(b_K\, \boldsymbol{Q}(K))$. The function b_K is the usual scalar bubble function associated to K, and $\boldsymbol{Q}(K)$ are properly chosen spaces such that the functions $\boldsymbol{v} \in \boldsymbol{H}(K)$ are characterized by the degrees of freedom defined by the functionals $\langle \hat{\boldsymbol{\eta}}^t, \boldsymbol{v} \rangle_{\partial K}$, $\boldsymbol{\eta}^t \in \boldsymbol{W}^t(\partial K)$.
4. A new FE pair $\boldsymbol{X}(K) \times \Psi(K)$ is defined such that $\boldsymbol{X}(K) = \boldsymbol{V}(K) \oplus \boldsymbol{H}(K)$.

As discussed in [16], stability of these FE pairs $\boldsymbol{X}_h(\boldsymbol{u}_D) \times \Psi_{0h}$ with respect to the norm

$$|||\boldsymbol{u}|||_h^2 := a_h(\boldsymbol{u}, \boldsymbol{v}) + M \|\nabla \cdot \boldsymbol{u}\|_{L^2(\Omega)}^2,$$

holds uniformly for Problem ($\mathrm{P_h}$), both for α and h parameters (where $M = \max\{\alpha, \mu\}$).

Lemma 2. Let $\mathcal{S}_h = \boldsymbol{X}_h \times \Psi_h \times \boldsymbol{\Lambda}_h^t \subset H(\mathrm{div}, \Omega) \times \Psi \times \boldsymbol{\Lambda}^t$ be a FE setting constructed by assembling local spaces $\boldsymbol{X}(K) \times \Psi(K) \times \boldsymbol{W}^t(\partial K)$ verifying the aforementioned properties. In this way, the FE pair $\boldsymbol{X}_h \times \Psi_h$ is divergence-consistent and $\boldsymbol{X}_h \times \boldsymbol{\Lambda}_h^t$ verifies the trace compatibility condition (22). Thus, the corresponding hybridized HM-H(div)($\mathcal{S}_h$) version for this method is also stable.

Proof. In fact, the enrichment procedure $\boldsymbol{X}(K) = \boldsymbol{V}(K) \oplus \boldsymbol{H}(K)$ by divergence-free bubble functions $\boldsymbol{H}(K)$ does not affect the divergence-consistency property and $\nabla \cdot \boldsymbol{X}(K) \subsetneqq \Psi(K)$ still holds. Moreover, since the degrees of freedom of $\boldsymbol{H}_h$ are characterized by the functionals defined by $\boldsymbol{\eta}_h^t \in \boldsymbol{\Lambda}_h^t$, and recalling that $\boldsymbol{H}_h \subset \boldsymbol{Z}_h(0)$, then the trace compatibility condition (22) holds uniformly with respect to the discretization parameters. □

5 | SOME ASPECTS IN COMPUTATIONAL IMPLEMENTATION

Considerable improvement in computational performance of HM-H(div)($\mathcal{S}_h$) formulations is achieved by the application of static condensation: the global system is solved only for a piecewise constant pressure variable, velocity normal trace and tangential traction over interfaces. Moreover, the use of a hierarchy of shape functions of high degree for a variety of element geometry, and appropriate data structure facilitates the implementation in the presence of complex mesh and geometry circumstances. These aspects are discussed in the following sections.

5.1 | Static condensation: reduced global system

Assembly and resolution of the full linear system associated to mixed methods demand elevated computational cost as compared with classic H^1-conforming methods, asking for optimized procedures to make the method competitive. Hybridization is a typical strategy adopted for application of a static condensation scheme to the system of equations. The degrees of freedom (DoF) of the problem are classified according to two sets of fields: the primal variables (solved globally) and the secondary variables (recovered locally from the primal ones). Usually, in FE methods the secondary variables correspond to terms that can be resolved independently within single elements (that can be condensed), and the primal ones involve contributions spread in more elements (they incorporate the global system to be solved).

For that, we introduce two new variables $\bar{p}_h \in \bar{\mathcal{P}}_h$ and $\bar{g}_h \in \bar{\mathcal{P}}_h$, playing the roles of element average pressure and element distributed flux, respectively. This way, the HM-H(div)($\mathcal{S}_h$) formulation can be expressed in the an equivalent form:

HM-H(div)($\mathcal{S}_h$): find $(\boldsymbol{u}_h, p_h, \bar{p}_h, \bar{g}_h, \lambda_h^t, \rho) \in \boldsymbol{X}_h \times \Psi_h \times \bar{\mathcal{P}}_h \times \bar{\mathcal{P}}_h \times \boldsymbol{\Lambda}_h^t \times \mathbb{R}$ satisfying the system

$$a_{\mathcal{T}_h}(\boldsymbol{u}_h, \boldsymbol{v}) + b(\boldsymbol{v}, p_h) + \langle \lambda_h^t, \boldsymbol{v} \rangle_{\partial \mathcal{T}_h} = (\boldsymbol{f}, \boldsymbol{v}), \tag{33}$$

$$b(\boldsymbol{u}_h, q) + (\bar{g}_h, q) + (\rho, q) = 0, \tag{34}$$

$$(\bar{\kappa}, p_h - \bar{p}_h) = 0, \tag{35}$$

$$\langle \boldsymbol{\eta}^t, \boldsymbol{u}_h \rangle_{\partial \mathcal{T}} = \langle \boldsymbol{\eta}^t, \boldsymbol{u}_D \rangle, \tag{36}$$

$$(\bar{g}_h, \bar{q}) = 0, \tag{37}$$

$$(\xi, p_h) = 0, \tag{38}$$

for all $(\boldsymbol{v}, q, \bar{q}, \bar{\kappa}, \boldsymbol{\eta}^t, \xi) \in \boldsymbol{X}_h \times \Psi_h \times \bar{\mathcal{P}}_h \times \bar{\mathcal{P}}_h \times \boldsymbol{\Lambda}^t \times \mathbb{R}$. Notice that the new variable $\bar{g}_h$ is a Lagrange multiplier introduced to enforce the solvability constraint $p_h - \bar{p}_h \in \Psi_h^{\perp}$.

For mixed formulations using $H(div)$-conforming approximations, the decomposition $\boldsymbol{X}_h = \boldsymbol{X}_h^{\partial} \oplus \mathring{\boldsymbol{X}}_h$ is helpful. This way, we express the velocity variable in the form $\boldsymbol{u}_h = \boldsymbol{u}_h^e + \boldsymbol{u}_h^i$, where the internal component $\boldsymbol{u}^i$ is of secondary type, being localized in single elements, whilst $\boldsymbol{u}^e$ is a primal variable, receiving influence for both sides of an element interface. Similarly, the pressure variable can be decomposed as $p_h = \bar{p}_h + p_h^{\perp} \in \bar{\mathcal{P}}_h \oplus \Psi_h^{\perp}$, where $p_h^{\perp}$ is also a secondary component and $\bar{p}_h$ a primary variable. After rearrangements of (33)-(38), splitting secondary and primary variables, the structure of the resulting local linear system

can be symbolically represented in each element K as (where the subscript h has been omitted for simplicity):

$$\begin{bmatrix} \boldsymbol{A}_{ii} & \boldsymbol{B}_{ip} & 0 & \boldsymbol{A}_{ie} & \mathbf{C}_{i\eta} & 0 & 0 \\ \boldsymbol{B}_{ip}^T & 0 & \mathbf{M} & \boldsymbol{B}_{ep}^T & 0 & 0 & \boldsymbol{D} \\ 0 & \mathbf{M}^T & 0 & 0 & 0 & \mathbf{G} & 0 \\ \boldsymbol{A}_{ie}^T & \boldsymbol{B}_{ep} & 0 & \boldsymbol{A}_{ee} & \mathbf{C}_{e\eta} & 0 & 0 \\ \mathbf{C}_{i\eta}^T & 0 & 0 & \mathbf{C}_{e\eta}^T & 0 & 0 & 0 \\ 0 & 0 & \mathbf{G} & 0 & 0 & 0 & 0 \\ 0 & \boldsymbol{D}^T & 0 & 0 & 0 & 0 & 0 \end{bmatrix} \begin{bmatrix} \hat{\mathbf{u}}_i \\ \hat{p} \\ \bar{g} \\ \hat{\mathbf{u}}_e \\ \hat{\lambda}^t \\ \bar{p} \\ \hat{\rho} \end{bmatrix} = \begin{bmatrix} R_i \\ 0 \\ 0 \\ R_e \\ R_\rho \\ 0 \\ 0 \end{bmatrix}. \tag{39}$$

Let $V_2 = (\hat{\boldsymbol{u}}_i, \hat{p}, \bar{g})^T$ and $V_1 = (\hat{\boldsymbol{u}}_e, \hat{\lambda}^t, \bar{p}, \hat{\rho})^T$ represent the DoF associated to secondary and primary variables, respectively. The block-matrices are

- $\mathbf{A}_{ii} \in \mathbb{R}^{n^i \times n^i}$, $\mathbf{A}_{ie} \in \mathbb{R}^{n^i \times n^e}$, $\mathbf{A}_{ee} \in \mathbb{R}^{n^e \times n^e}$, $\mathbf{B}_{ip} \in \mathbb{R}^{n^i \times n^p}$, $\mathbf{B}_{ep} \in \mathbb{R}^{n^e \times n^p}$,
- $\mathbf{B}_{e\bar{p}} \in \mathbb{R}^{n^e \times \bar{n}}$, $\mathbf{G} \in \mathbb{R}^{\bar{n} \times \bar{n}}$, $\mathbf{C}_{i\eta} \in \mathbb{R}^{n^i \times n^\eta}$, $\mathbf{C}_{e\eta} \in \mathbb{R}^{n^e \times n^\eta}$, $\mathbf{M} \in \mathbb{R}^{n^p \times \bar{n}}$,
- $D \in \mathbb{R}^{n^p}$, $R_i \in \mathbb{R}^{n^i}$, $R_e \in \mathbb{R}^{n^e}$, $R_\rho \in \mathbb{R}^{n^\eta}$,

where: n^i = number of internal velocity shape functions, n^e = number of border velocity shape functions, n^p = number of pressure shape functions, $\bar{n}$ = number of local average pressure shape functions, and n^η=number of Lagrange multiplier shape functions.

By expressing (39) in the compact block form

$$\begin{bmatrix} K_{11} & K_{12} \\ K_{21} & K_{22} \end{bmatrix} \begin{bmatrix} V_2 \\ V_1 \end{bmatrix} = \begin{bmatrix} R_2 \\ R_1 \end{bmatrix},$$

the primary variable V_1 is the solution of the reduced system

$$\left[K_{22} - K_{21}K_{11}^{-1}K_{12}\right] V_1 = R_1 - K_{21}K_{11}^{-1}R_2.$$

After the computation of the primary variable V_1 solving the global system obtained by the assembly of these local primary systems, the secondary variable V_2 is recovered by independent local solvers $V_2 = K_{11}^{-1}(R_2 - K_{12}V_1)$ in each element K.

5.2 | Computational framework

The hybridization strategy requires the construction of approximation spaces for velocity, pressure, Lagrange multiplier and normal velocity trace, including the respective DoF. For each element K, we also include the DoF associated with the average pressure $\bar{p}$ and distributed flux $\bar{g}$. Some aspects of a mesh partition $\mathcal{T}_h$ are displayed in Figure 2. Over the mesh skeleton Γ_h, interface elements are created linking the DoF of $\boldsymbol{\lambda}^t$ and $\boldsymbol{u}$ (for velocities in each element K side), which weakly impose the terms $\langle \boldsymbol{\lambda}_h^t, \boldsymbol{v} \rangle_{\partial\mathcal{T}}$ and $\langle \boldsymbol{\eta}^t, \boldsymbol{u}_h^e + \boldsymbol{u}_h^i \rangle_{\partial\mathcal{T}}$, respectively in Eqs. (33) and (36). For the boundary condition, the same procedure is adopted.

Results of numerical simulations of the HM-H(div)(S_h) method presented in the next section were implemented using object-oriented programming principles and robust and flexible computational tools of the open-source library NeoPZ [1]. Some of the distinct features of the library used for implementing and generating the results are:

- *TPZGeoElRefPattern* allow to divide elements uniformly or directionally.
- For the construction of the required divergence consistent FE pairs, a hierarchy of shape functions $\hat{\boldsymbol{\varphi}}$ of high degree for a variety of reference element geometry are employed. Proposed in [43,44,41], they are defined in the form $\hat{\boldsymbol{\varphi}} = \hat{\varphi}\,\hat{\boldsymbol{v}}$, multiplying hierarchical scalar basis functions $\hat{\varphi}$ for subspaces in $H^1(\hat{K})$ by properly chosen constant vector fields $\hat{\boldsymbol{v}}$.
- *TPZArc3D* together with *TPZGeoBlend* allow to represent circular boundaries within machine precision. *TPZGeoBlend* is designed for the calculation of directions and gradients associated to H(div)-conforming approximations. The gradient of the shape function $\hat{\boldsymbol{\varphi}} = \hat{\varphi}\,\hat{\boldsymbol{v}}$, is defined by the expression

$$\nabla\hat{\boldsymbol{\varphi}} = \hat{\varphi}\nabla\hat{\boldsymbol{v}} + \hat{\boldsymbol{v}} \otimes \nabla\hat{\varphi}. \tag{40}$$

[1] NeoPZ open-source platform: http://github.com/labmec/neopz

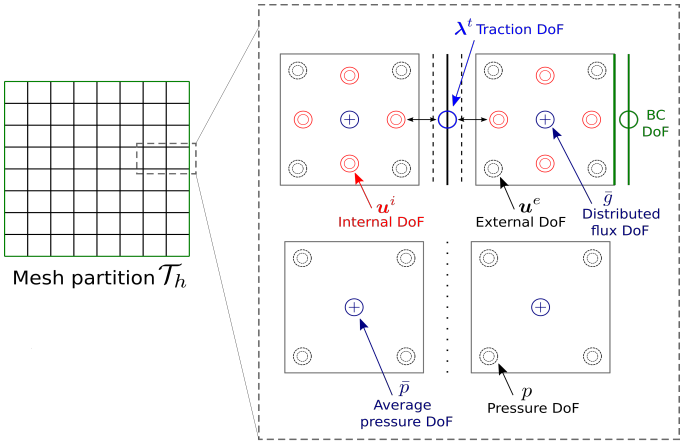

Figure 2 Mesh aspects for computational implementation of hybrid schemes.

- Computing the gradient H(div) functions requires computing the second derivative of the geometric map. Automatic differentiation was used to compute the gradient of H(div) functions.

A proper data structure is also available in NeoPZ allowing implementation of H^1 and H(div)-conforming spaces with trace constraints over interfaces, without limitations on hanging sides and distribution of approximation orders, as demonstrated in [45,46,47,48] for hp-adaptive applications and in [49] for multiscale simulations of Darcy flows.

6 | NUMERICAL VERIFICATION TESTS

In this section, we present and discuss some numerical test models to illustrate the approximation properties of the semi-hybrid-mixed formulation discussed in the previous sections. The convergence histories are presented for errors of the variables measured by L^2-norms, simply denoted by $\|\cdot\|$ in all the cases.

6.1 | 2D models for conformal affine partitions

The Brinkman-Stokes test problems proposed in [50] defined in the rectangular domain $\Omega = (0,2)\times(-1,1)$ is considered. Taking $C = C(\alpha,\mu) = \alpha\mu^{-1}$, and $\chi(\xi) = \exp(\xi)^{-1}$, $\xi \in \mathbb{R}^+$ (with $\chi(+\infty) = 0$), the exact solutions $\boldsymbol{u} = \chi(C)\,\boldsymbol{u}^S + (1-\chi(C))\,\boldsymbol{u}^D$, $p = \cos x \sin y - p_0$ hold for the problems in the whole range of parameters, where $p_0 \in \mathbb{R}$ is such that the zero average $p \in L^2_0(\Omega)$ is verified. We present numerical results for the Brinkman problem with $(\mu,\alpha) = (1,1)$, and for the limit cases $(\mu,\alpha) = (1,0)$ (Stokes) and $(\mu,\alpha) = (0,1)$ (Darcy), with corresponding velocity fields

$$\boldsymbol{u}^S = \nabla\times\psi, \quad \text{where} \quad \psi = -\sin x\cos y, \tag{41}$$

$$\boldsymbol{u}^D = -\nabla p, \tag{42}$$

$$\boldsymbol{u}^B = e^{-1}\,\boldsymbol{u}^S + (1-e^{-1})\,\boldsymbol{u}^D. \tag{43}$$

Boundary and source data are obtained from the expressions of these exact solutions.

6.1.1 | Convergence histories for the HM-H(div)(S_h) method

Uniform conformal meshes $\mathcal{T}_h = \{K\}$ of triangular or quadrilateral elements K are considered, with mesh size $h = 2/N$, $N = 2^i$, $i = 2,\cdots 6$. Based on these meshes, we consider FE spaces of type H(div)$(h, S_{h,RT(k)})$ for quadrilaterals and $S_{h,BDM^+(k)}$ for triangles, with $k = 1, 2$, and 3, with polynomial trace spaces having degree $m = k-1$.

The L^2-errors for $\boldsymbol{u}$, $\nabla\cdot\boldsymbol{u}$, and p are presented in Table 4 (top side) for the Stokes problem obtained by the formulations HM-H(div)$(h, S_{h,RT(k)})$ (left side) and HM-H(div)$(h, S_{h,BDM^+(k)})$ (right side). Optimal convergence rates of order $k+1$ are reached for the velocity variable for all FE space configurations. The observed pressure rates are of order k for the $S_{h,BDM^+(k)}$ model, but

an improved order $k+\frac{1}{2}$ occurs for the $S_{h,RT(k)}$ space setting. For all simulations, the L^2-errors of $\nabla \cdot \boldsymbol{u}$ illustrate the strongly enforced divergence-free property.

The results for the Brinkman problem presented in Table 4 (bottom side) show similar convergence behavior for velocity and pressure, excepting that the improved rates of order $k+\frac{1}{2}$ for pressure using the $S_{h,RT(k)}$ space configuration is only observed for odd k. For the Brinkman problem, optimal convergence rate of order $k+1$ is verified.

In Figure 3 the effect of static condensation is verified in terms of the size of the global system to be solved with respect to the total number of unknowns for $N = 64$. For all the methods, the reduction is more significant with increasing order of approximation and for rectangular meshes, for which the condensed equations amounts to about 80% when $k = 5$.

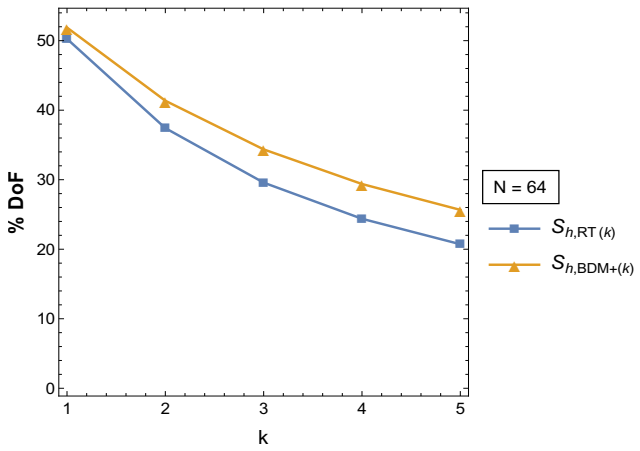

Figure 3 Percentage of degrees-of-freedom in the global system at the refinement level $N = 64$ used to solve the Stokes problem by the formulations HM-H(div)($S_{h,RT(k)}$) and HM-H(div)($S_{h,BDM^+(k)}$) applied to quadrilateral and triangular meshes.

6.1.2 | Comparison results of HM-H(div)(S_h) with respect to DG methods

The errors for $\boldsymbol{u}$ and p of the Stokes problem shown in Table 4 for the HM-H(div)($S_{RT(3)}$) method are plotted in Figure 4. For comparison, corresponding error curves given by two versions of the symmetric Discontinuous Galerkin method are included as well. Namely, $RT^{DG}(k)$ and $RT^{\mathrm{div},DG}(k)$ methods, where the indexes DG and div, DG are used to distinguish the DG methods using fully discontinuous or H(div)-conforming velocity spaces (see [13] and references therein).

Notice that velocity and pressure spaces of all methods coincide on the reference element, but they differ in their assembly strategies. Similarly, comparison results for the HM-H(div)($S_{h,BDM^+(3)}$) formulation with respect to the corresponding symmetric Discontinuous Galerkin methods $BDM^{+,DG}(3)$ and $BDM^{+,\mathrm{div},DG}(3)$, based on triangular meshes, are plotted in Figure 4 (bottom side).

The velocity convergence rates of order $k+1$ occur for all DG and HM-H(div)(S_h) formulations, the error curves being quite similar. However, convergence histories for pressure improves significantly when hybridization is applied, as compared to the DG methods.

Similar behavior occurs for Brinkman problems, as illustrated in Fig. 5, where the results are for the symmetric DG methods $BDM^{+,DG}(k)$ and $BDM^{+,\mathrm{div},DG}(k)$, and for the HM-H(div)($S_{h,BDM^+(k)}$) formulation based on triangular meshes for $k = 2$ and 3.

In the illustrations shown in Figure 6, it can be observed that there is a significant impact in using static condensation for the reduction of the number of equations to be solved in the semi-hybrid-mixed formulations as compared with DG methods.

It should be noted that matrix bandwidth for DG methods are typically large and static condensation is not allowed, while for the HM-H(div)(S_h) formulations the matrix bandwidth of the reduced condensed system is considerably smaller, leading to increased numerical efficiency. Moreover, the exact divergence-free property of velocity fields approximated in H(div)-conforming velocity FE spaces is not verified by fully discontinuous DG methods.

Table 4 Stokes $(\mu, \alpha) = (1, 0)$ and Brinkman $(\mu, \alpha) = (1, 1)$ model problems: convergence history for $\boldsymbol{u}$, $\nabla \cdot \boldsymbol{u}$, and p, given by the formulations HM-H(div)($S_{h,RT(k)}$) (left side) and HM-H(div)($S_{h,BDM^+(k)}$)(right side), with $m = k - 1$, and $h = 2/N$.

	Quadrilateral elements: $S_{h,RT(k)}$			Triangular elements: $S_{h,BDM^+(k)}$		
Stokes problem $(\mu, \alpha) = (1, 0)$						
N	$\|\boldsymbol{u} - \boldsymbol{u}_h\|$	$\|p - p_h\|$	$\|\nabla \cdot (\boldsymbol{u} - \boldsymbol{u}_h)\|$	$\|\boldsymbol{u} - \boldsymbol{u}_h\|$	$\|p - p_h\|$	$\|\nabla \cdot (\boldsymbol{u} - \boldsymbol{u}_h)\|$
	$k = 1$					
4	$1.91E-02$	$4.54E-02$	$5.57E-15$	$5.11E-02$	$2.61E-01$	$1.35E-14$
8	$4.75E-03$	$1.61E-02$	$1.33E-14$	$1.31E-02$	$1.35E-01$	$3.20E-14$
16	$1.18E-03$	$5.68E-03$	$2.02E-14$	$3.33E-03$	$6.83E-02$	$6.90E-14$
32	$2.96E-04$	$2.01E-03$	$4.26E-14$	$8.38E-04$	$3.43E-02$	$1.49E-13$
64	$7.39E-05$	$7.10E-04$	$1.15E-14$	$2.10E-04$	$1.72E-02$	$1.47E-14$
Rate	2.00	1.50	-	2.00	1.00	–
N	$k = 2$					
4	$1.37E-03$	$3.45E-03$	$2.93E-15$	$3.03E-03$	$2.35E-02$	$7.10E-14$
8	$1.70E-04$	$7.83E-04$	$8.76E-15$	$3.81E-04$	$6.09E-03$	$6.45E-15$
16	$2.12E-05$	$1.56E-04$	$1.49E-14$	$4.80E-05$	$1.54E-03$	$1.41E-14$
32	$2.65E-06$	$2.93E-05$	$3.05E-14$	$6.02E-06$	$3.87E-04$	$2.83E-14$
64	$3.31E-07$	$5.31E-06$	$6.03E-14$	$7.55E-07$	$9.68E-05$	$5.54E-14$
Rate	3.00	2.46	–	3.00	2.00	–
N	$k = 3$					
4	$2.83E-05$	$1.49E-04$	$6.75E-15$	$1.61E-04$	$1.40E-03$	$7.55E-15$
8	$1.77E-06$	$1.30E-05$	$1.21E-14$	$9.64E-06$	$1.62E-04$	$1.32E-14$
16	$1.10E-07$	$1.15E-06$	$2.55E-14$	$5.88E-07$	$1.94E-05$	$2.71E-14$
32	$6.87E-09$	$1.01E-07$	$5.18E-14$	$3.63E-08$	$2.37E-06$	$5.50E-14$
64	$4.29E-10$	$8.96E-09$	$9.96E-14$	$2.26E-09$	$2.93E-07$	$1.09E-13$
Rate	4.00	3.50	–	4.01	3.02	–
Brinkman problem $(\mu, \alpha) = (1, 1)$						
N	$\|\boldsymbol{u} - \boldsymbol{u}_h\|$	$\|p - p_h\|$	$\|\nabla \cdot (\boldsymbol{u} - \boldsymbol{u}_h)\|$	$\|\boldsymbol{u} - \boldsymbol{u}_h\|$	$\|p - p_h\|$	$\|\nabla \cdot (\boldsymbol{u} - \boldsymbol{u}_h)\|$
	$k = 1$					
4	$1.60E-02$	$3.34E-02$	$1.09E-02$	$1.90E-02$	$1.16E-01$	$2.07E-02$
8	$3.97E-03$	$1.18E-02$	$2.76E-03$	$4.85E-03$	$5.90E-02$	$5.20E-03$
16	$9.90E-04$	$4.15E-03$	$6.92E-04$	$1.23E-03$	$2.97E-02$	$1.30E-030$
32	$2.47E-04$	$1.47E-03$	$1.73E-04$	$3.08E-04$	$1.49E-02$	$3.26E-04$
64	$6.18E-05$	$5.18E-04$	$4.33E-05$	$7.73E-05$	$7.45E-03$	$8.14E-05$
Rate	2.00	1.50	2.00	2.00	1.00	2.00
N	$k = 2$					
4	$9.88E-04$	$4.07E-03$	$6.74E-04$	$1.19E-03$	$1.16E-02$	$1.36E-03$
8	$1.23E-04$	$9.99E-04$	$8.42E-05$	$1.49E-04$	$2.93E-03$	$1.72E-04$
16	$1.54E-05$	$2.38E-04$	$1.05E-050$	$1.88E-05$	$7.30E-04$	$2.15E-05$
32	$1.92E-06$	$5.72E-05$	$1.31E-06$	$2.35E-06$	$1.82E-04$	$2.69E-06$
64	$2.40E-07$	$1.39E-05$	$1.64E-07$	$2.95E-07$	$4.54E-05$	$3.36E-07$
Rate	3.00	2.04	3.00	3.00	2.00	3.00
N	$k = 3$					
4	$2.31E-05$	$1.16E-04$	$1.45E-05$	$6.01E-05$	$5.42E-04$	$8.30E-05$
8	$1.44E-06$	$1.01E-05$	$9.18E-07$	$3.59E-06$	$6.18E-05$	$5.21E-06$
16	$9.00E-08$	$8.93E-07$	$5.75E-08$	$2.19E-07$	$7.34E-06$	$3.26E-07$
32	$5.62E-09$	$7.88E-08$	$3.60E-09$	$1.36E-08$	$8.95E-07$	$2.04E-08$
64	$3.51E-10$	$6.96E-09$	$2.25E-10$	$8.43E-10$	$1.10E-07$	$1.27E-09$
Rate	4.00	3.50	4.00	4.01	3.02	4.00

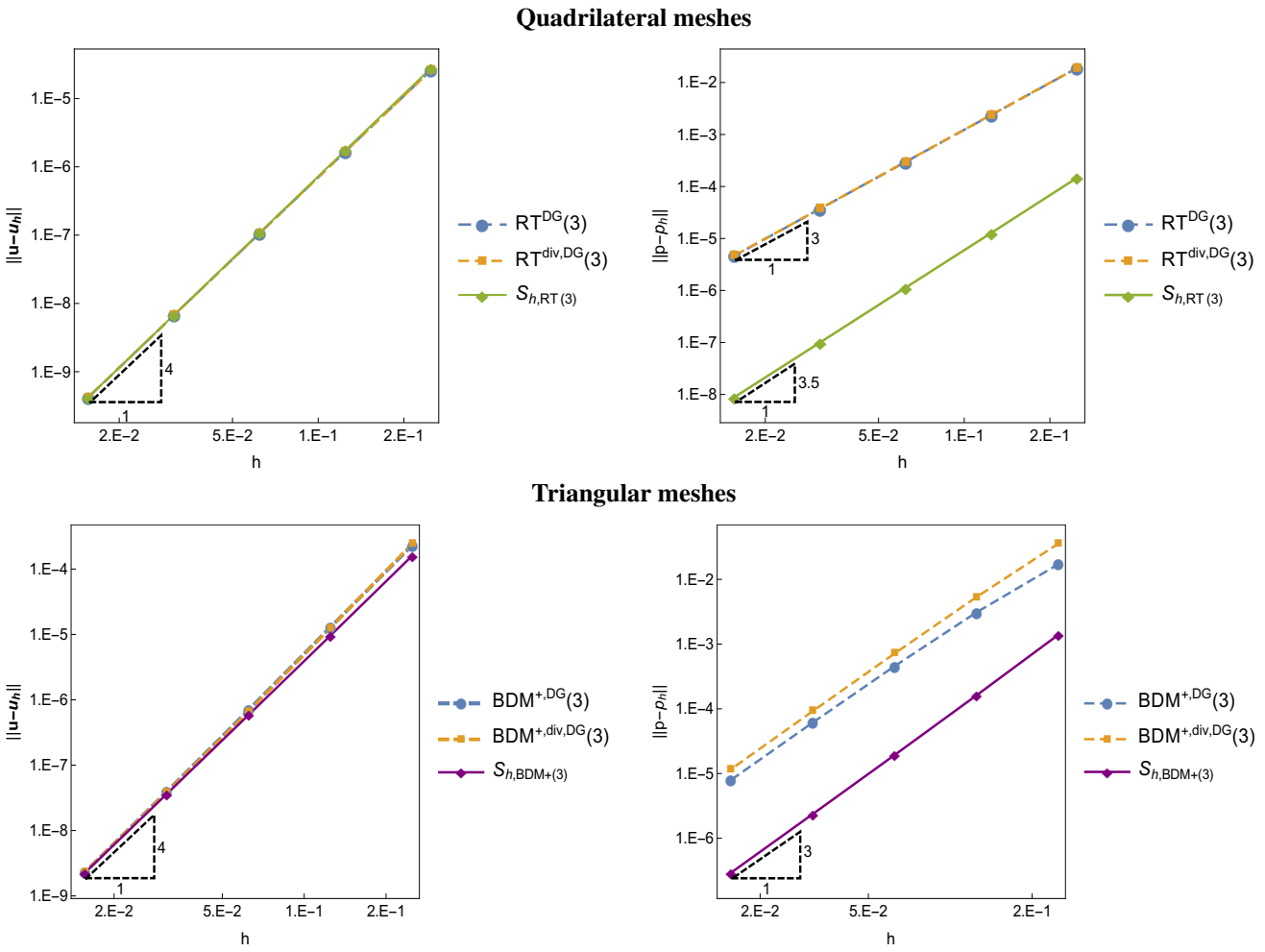

Figure 4 Stokes problem $(\mu, \alpha) = (1, 0)$: convergence history for $\boldsymbol{u}$ (left side) and p (right side), obtained with symmetric DG methods $RT^{DG}(3)$ and $RT^{\text{div},DG}(3)$, and with the HM-H(div)($S_{h,RT(3)}$) formulation based on quadrilateral meshes (top); Similar error curves for the symmetric DG methods $BDM^{+,DG}(3)$ and $BDM^{+,\text{div},DG}(3)$, and for the HM-H(div)($S_{h,BDM^{+}(3)}$) formulation based on triangular meshes (down).

6.2 | Pressure-robustness verification

Pressure-robustness is an important feature of numerical methods for fluid flows, meaning that an external perturbation in the source term, which influences only the pressure in the stress equilibrium, affects only the pressure in the discrete equations as well. In order to exemplify this property for the the HM-H(div)(S_h) method, let us considered Stokes problems in the domain $\Omega = (0, 1) \times (0, 1)$, $\boldsymbol{u} = 0$ with no-slip boundary conditions. We set a no-flow problem $\boldsymbol{u} = 0$ with $\mu = 1$, the pressure exact solution $p = m_{pr}(y^3 - y^2/2 + y - 7/12)$ and the source term $\boldsymbol{f} = (0, m_{pr}(1 - y + 3y^2))$ using a parameter $m_{pr} > 0$. This model problem was evaluated in[51] to illustrate the lack of pressure-robustness of the standard conforming Taylor-Hood, and mini methods, and of the nonconforming Crouzeix–Raviart method.

For numerical approximations by the HM-H(div)(S_h) method, we consider uniform meshes $\mathcal{T}_h = \{K\}$ of triangular or quadrilateral elements K, with mesh size $h = 1/N$, $N = 2^i$, $i = 2, \cdots 7$. The results for velocity and pressure fields obtained by using FE configurations of types $S_{h,RT(k)}$ and $S_{h,BDM^{+}(k)}$ are plotted in Figure 7, for $k = 2$ and $m = 1$. The L^2-norm errors of $\nabla \cdot \boldsymbol{u}$ are listed in Table 5 for all simulations. The pressure-robustness is verified when we impose a variation in the parameter m_{pr}, which has a direct impact in the pressure error with a significant increase in its magnitude, as expected. Without significant influence of velocity and consistency errors, the pressure errors recover the optimal convergence rate of order $k + 1$. In terms of the velocity error, we observe the divergence-free property and a reduced error magnitude explained by the machine precision in the numerical computations.

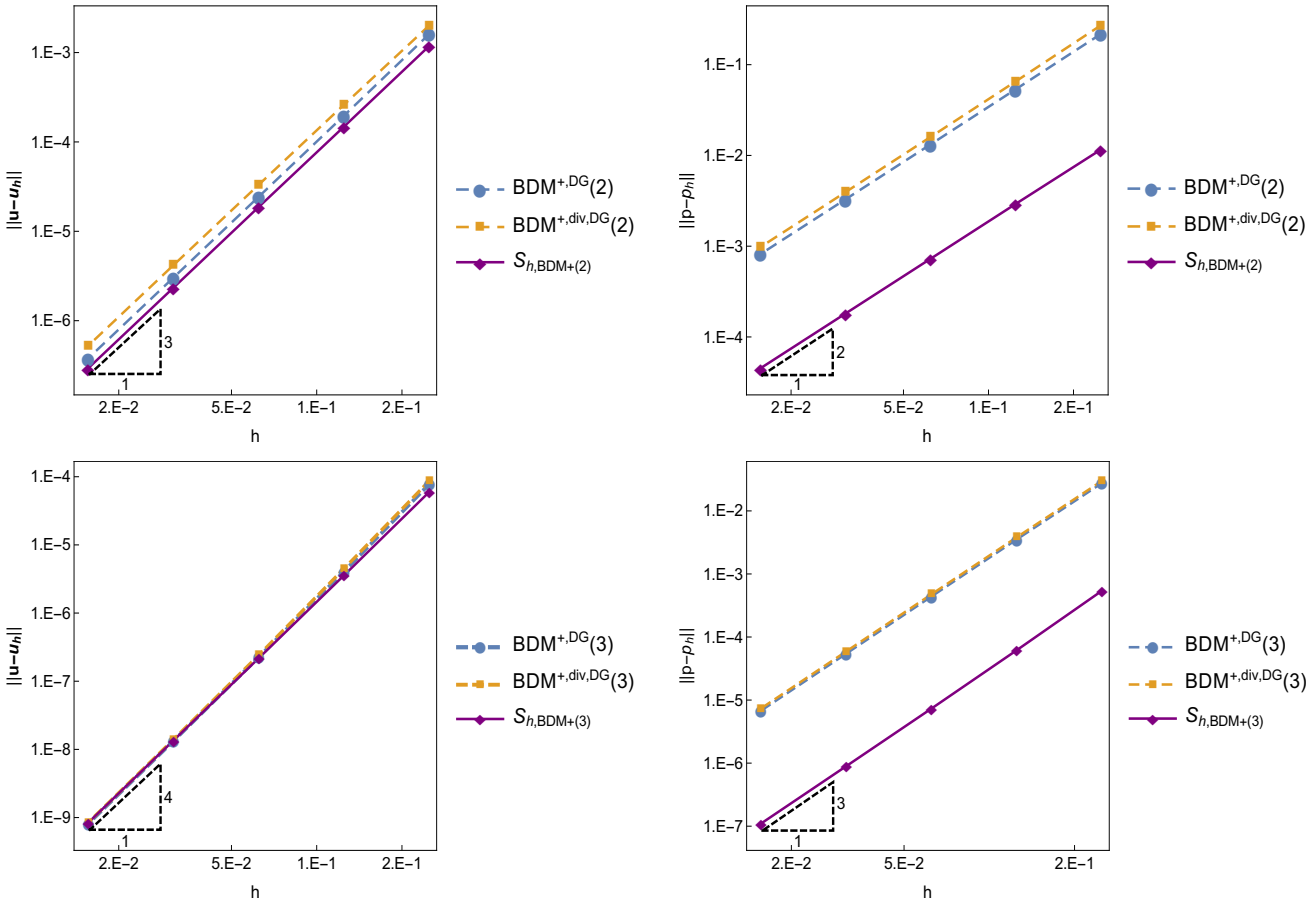

Figure 5 Brinkman problem, $(\mu, \alpha) = (1, 1)$: convergence history for $\boldsymbol{u}$ (left side) and p (right side), obtained with symmetric DG methods $BDM^{+,DG}(k)$ and $BDM^{+,\mathrm{div},DG}(k)$, and for the HM-H(div)($S_{h,BDM^+(k)}$) formulation based on triangular meshes for $k = 2$ (top) and 3 (down).

Table 5 Pressure-robustness verification: $\|\nabla \cdot (\boldsymbol{u} - \boldsymbol{u}_h)\|$ for multiplying factors m_{pr}, obtained with the HM-H(div)($S_{h,RT(k)}$) and HM-H(div)($S_{h,BDM^+(k)}$) formulations with $k = 2$, $h = 1/N$, and Lagrange multiplier of degree $m = 1$.

N	$S_{h,RT(k)}$				$S_{h,BDM^+(k)}$			
	$m_{pr} = 1$	$m_{pr} = 100$	$m_{pr} = 10^4$	$m_{pr} = 10^6$	$m_{pr} = 1$	$m_{pr} = 100$	$m_{pr} = 10^4$	$m_{pr} = 10^6$
4	$4.95E-17$	$4.69E-15$	$4.65E-13$	$4.55E-11$	$3.70E-17$	$4.02E-15$	$3.64E-13$	$3.61E-11$
8	$5.22E-17$	$5.28E-15$	$5.20E-13$	$4.99E-11$	$3.53E-17$	$3.47E-15$	$3.60E-13$	$3.48E-11$
16	$5.02E-17$	$5.01E-15$	$5.00E-13$	$5.01E-11$	$3.34E-17$	$3.41E-15$	$3.39E-13$	$3.36E-11$
32	$4.87E-17$	$4.86E-15$	$4.87E-13$	$4.86E-11$	$3.35E-17$	$3.36E-15$	$3.36E-13$	$3.33E-11$
64	$4.99E-17$	$4.99E-15$	$4.99E-13$	$4.99E-11$	$3.32E-17$	$3.32E-15$	$3.34E-13$	$3.33E-11$
128	$5.13E-17$	$5.13E-15$	$5.13E-13$	$5.12E-11$	$2.18E-16$	$5.35E-15$	$1.55E-12$	$2.34E-10$

6.3 | Brinkman problems in Darcy limit

A numerical verification is proposed for the Brinkman problem close the limit Darcy regime, which can be a critical flow situation. The Brinkman problem with the exact solution (43) for $\alpha = 1$ and viscosity values $\mu = 10^{-5}, 10^{-6}$ and 10^{-7} are simulated with the methods HM-H(div)($S_{h,RT(k)}$) and HM-H(div)($S_{h,BDM^+(k)}$), based on uniform quadrilateral and triangular meshes, respectively. The L^2-errors in $\boldsymbol{u}$ and p are represented graphically in Figs. 8 for the different viscosity cases. For each

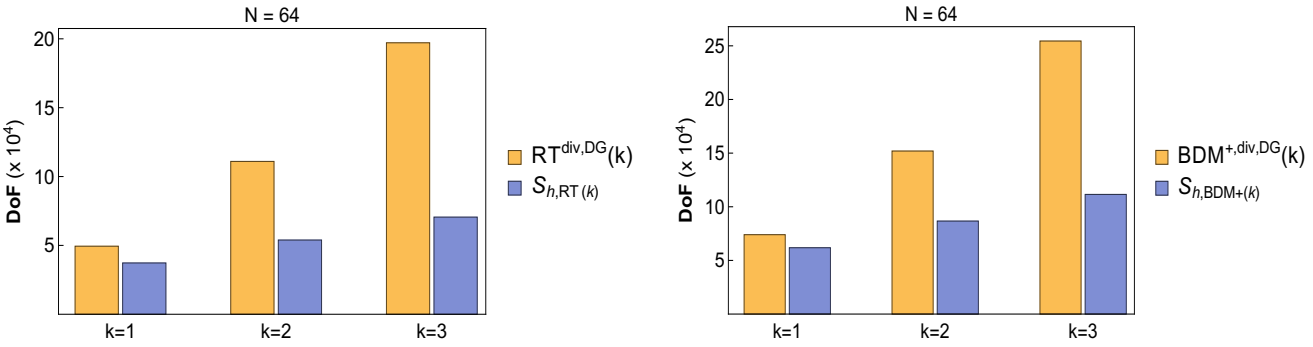

Figure 6 Stokes $(\mu, \alpha) = (1, 0)$ and Brinkman $(\mu, \alpha) = (1, 1)$ model problems: number of equations solved with symmetric DG methods $RT^{\text{div},DG}(k)$, and with the HM-H(div)($S_{h,RT(k)}$) formulation based on quadrilateral meshes (left); Similar plots for the symmetric DG methods $BDM^{+,\text{div},DG}(k)$, and for the HM-H(div)($S_{h,BDM^{+}(k)}$) formulation based on triangular meshes, with spacing $h = 1/32$.

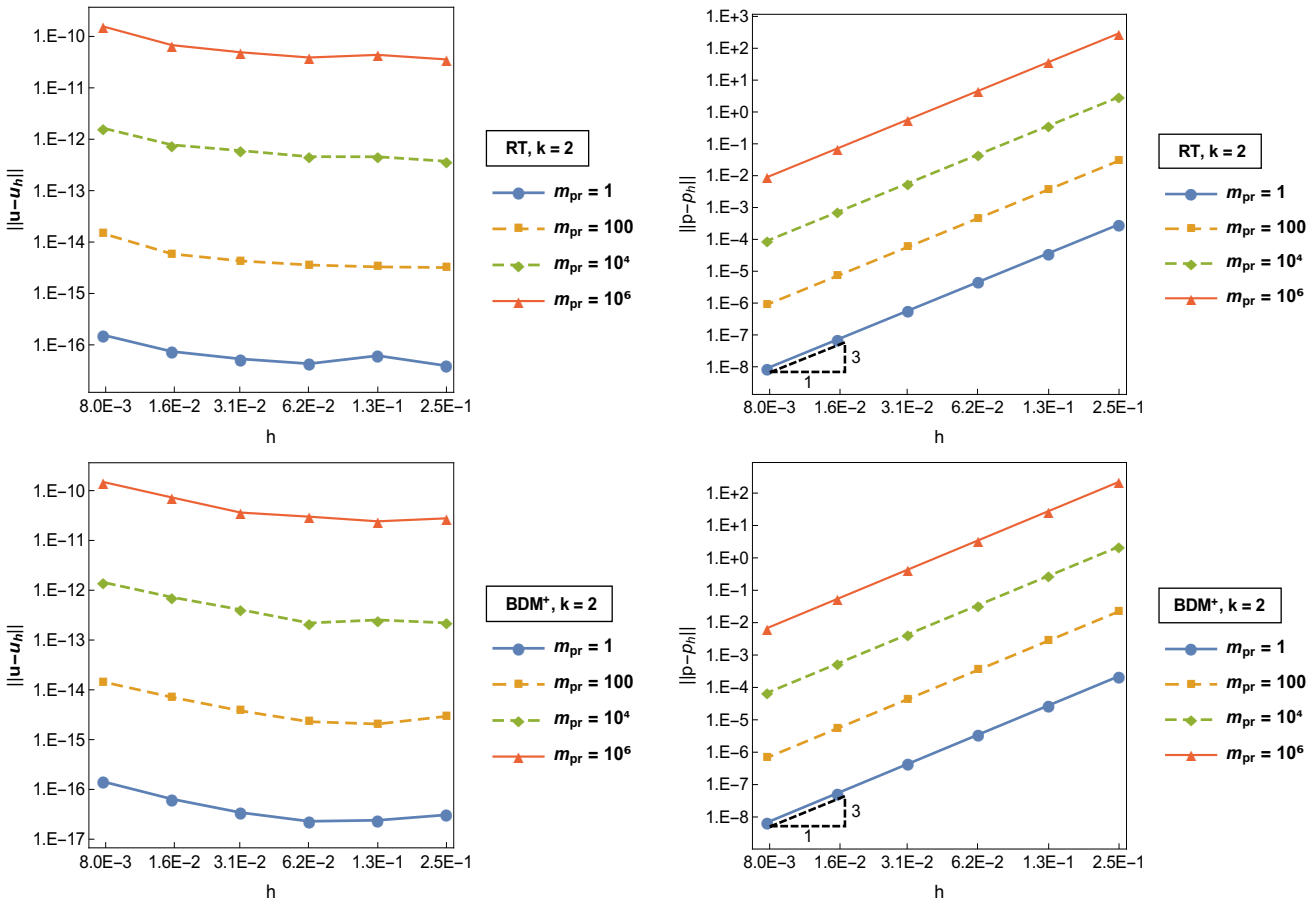

Figure 7 Pressure-robustness verification: convergence history for $\boldsymbol{u}$ (left side) and p (right side), obtained with the HM-H(div)($S_{h,RT(k)}$) method for quadrilateral elements (top) and the HM-H(div)($S_{h,BDM^{+}(k)}$) method for triangular elements (bottom), with $k = 2$ and Lagrange multiplier degree $m = 1$.

$k = 1, 2$, and 3, the error curves for the different viscosity values are quite similar, showing convergence rates of order $k + 1$, which are typical of the mixed formulation in the Darcy limit corresponding to the parameters $(0, \alpha)$.

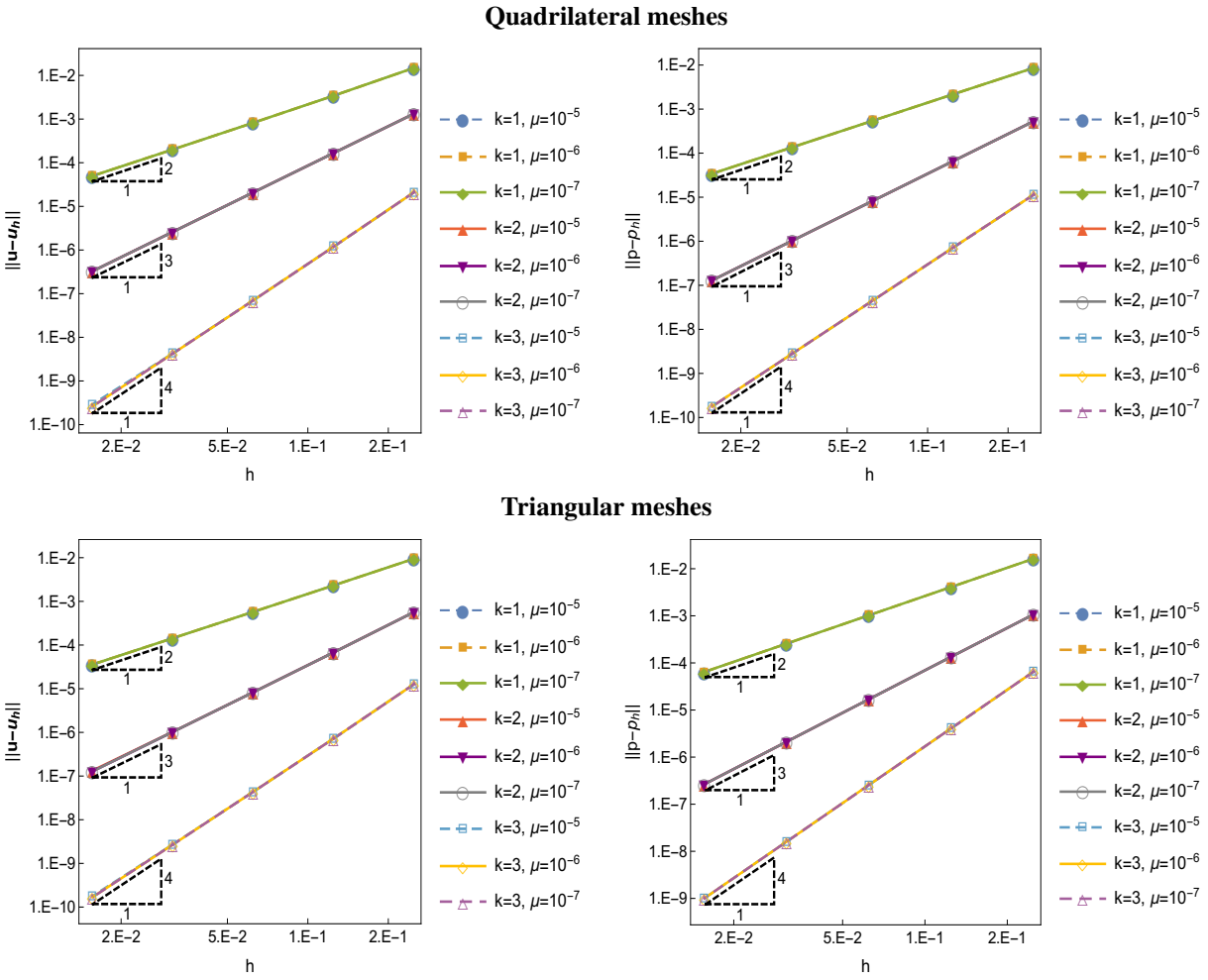

Figure 8 Brinkman problem $(1, \mu)$ in Darcy limit, with $\mu = 10^{-5}, 10^{-6}$ and 10^{-7}: convergence history for $\boldsymbol{u}$ (left side) and p (right side), obtained with the formulations HM-H(div)($S_{h,RT(k)}$) (top side) and HM-H(div)($S_{h,BDM^+(k)}$)(bottom side), $k = 1, 2, 3$.

6.4 | Stokes flows in the presence of more complex meshes and domain geometry

Here, we apply the new semi-hybrid mixed scheme to compute Stokes flows in more complex meshes and domain geometry. Namely, we treat non-conforming meshes with irregular refinement patterns, a flow in a curved domain, and in a domain with circular obstacles.

6.4.1 | Non-conforming meshes with local refinement patterns

The first case is for the Stokes solution (41) computed in non-conforming meshes denoted by QS, for quadrilateral elements, and TS1, for triangular ones. These two types of meshes are based on a coarse partition with spacing $h = 2/N, N = 2^i, i = 2, \cdots 6$ complemented with internal refinements, as represented in Figs. 9. For the numerical approximations, h-adapted space configurations are used of type $S_{h,RT(k)}$ for the quadrilateral non-conforming meshes, and $S_{h,BDM^+(k)}$ for triangular ones, with $k = 1, 2$, and 3. In all the cases, the one-dimensional elements composing the Lagrange multiplier space are based on the coarse partition level and using polynomials of degree $k - 1$.

The L^2 approximation errors in $\boldsymbol{u}$, p and $\nabla \cdot \boldsymbol{u}$ and the corresponding rates of convergence with respect to h are indicated in Table 6. Similarly to the cases of conformal uniform partitions, optimal convergence rate of order $k + 1$ is observed for the velocity variable and the pressure rate is of order k. The error estimation for $\nabla \cdot \boldsymbol{u}$ with L^2-norm indicates the strong enforcement of the divergence-free property by this method.

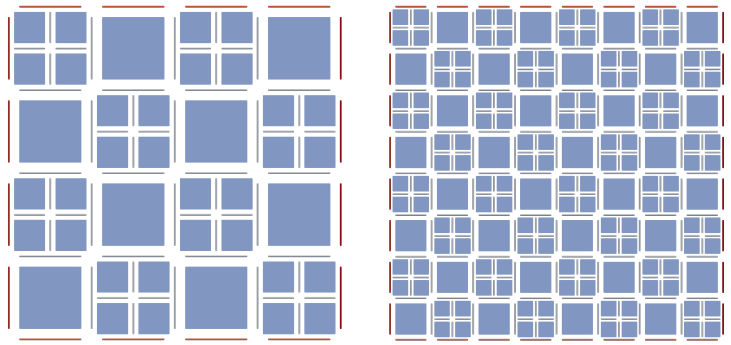

(a) $h = 2/4$ (b) $h = 2/8$

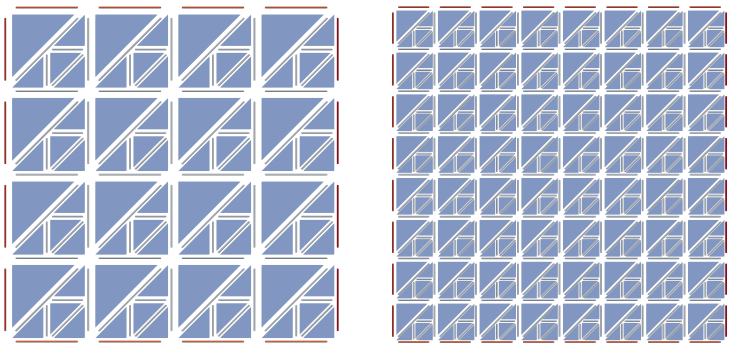

(c) $h = 2/4$ (d) $h = 2/8$

Figure 9 Non-conforming meshes with regular refinement pattern and spacing h: quadrilateral elements of type QS (figures (a) and (b)); triangular elements of type TS (figures (c) and (d)).

6.4.2 | Application to a curved domain:

The verification of the semi-hybrid-mixed formulation is now extended to a curvilinear region and deformed element meshes. For this analysis, the Stokes problem is defined in the domain Ω bounded by the following curves:

$$\Gamma_1 = \{\mathbf{x} = (x, y) \in \mathbb{R}^2 \,:\, 0.5 \leq x \leq 1.0, y = 0\},$$
$$\Gamma_2 = \{\mathbf{x} = (x, y) \in \mathbb{R}^2 \,:\, \|\mathbf{x}\|^2 = 1.0\},$$
$$\Gamma_3 = \{\mathbf{x} = (x, y) \in \mathbb{R}^2 \,:\, x = 0, 0.5 \leq y \leq 1.0\},$$
$$\Gamma_4 = \{\mathbf{x} = (x, y) \in \mathbb{R}^2 \,:\, \|\mathbf{x}\|^2 = 0.5\},$$

with slip boundary condition, as illustrated in Figs. 10(a) and 10(b). For viscosity $\mu = 1$, the exact velocity, expressed in polar coordinates, is $\mathbf{u}_{exact} = -rsin\theta\,\mathbf{i} + rcos\theta\,\mathbf{j}$ (see Fig. 10(c)). The boundary conditions are imposed on a computational boundary, which is built to be coincident with the physical boundary. We remark that the geometric mappings are implemented, as described in[41,52], by the transfinite interpolation methodology[53]. For this case, a quadrilateral reference domain is mapped onto a curved bounded region. Besides, in order to obtain an efficient computation of the gradient of velocity shape function (40), we implement a non-linear transformation using the Forward Automatic Differentiation (FAD), allowing an object to store the vector and its derivatives.

The velocity value is weakly imposed using a Dirichlet boundary condition, considering the tangential component as the only contribution to be added to the problem formulation:

$$\langle \boldsymbol{\eta}^t, \boldsymbol{u}_D \rangle_{\partial\Omega_D} = \langle \boldsymbol{\eta}^t \cdot \boldsymbol{t}, \boldsymbol{u}_D \cdot \boldsymbol{t} \rangle_{\partial\Omega_D} = \langle \boldsymbol{\eta}^t \cdot \boldsymbol{t}, r \rangle_{\partial\Omega_D}, \tag{44}$$

where $r = r_i$ for internal radius and $r = r_e$ for external radius, as shown in Fig. 10. Please note that $\boldsymbol{u}_D \cdot \boldsymbol{t} = 0$ for bottom and top boundary conditions.

Table 6 Stokes problem solved with non-conforming quadrilateral meshes QS and triangular meshes TS: L^2-errors in $\boldsymbol{u}$, p and $\nabla \cdot \boldsymbol{u}$ obtained with the space configuration $S_{h,RT(k)}$, and $S_{h,BDM^+(k)}$, respectively, with spacing $h = 2/N$, and $k = 1, 2, 3$.

Quadrilateral QS meshes				Triangular TS meshes		
$k = 1$						
N	$\|\boldsymbol{u} - \boldsymbol{u}_h\|$	$\|p - p_h\|$	$\|\nabla \cdot (\boldsymbol{u} - \boldsymbol{u}_h)\|$	$\|\boldsymbol{u} - \boldsymbol{u}_h\|$	$\|p - p_h\|$	$\|\nabla \cdot (\boldsymbol{u} - \boldsymbol{u}_h)\|$
4	$1.59E-02$	$8.95E-02$	$1.11E-15$	$4.98E-02$	$2.78E-01$	$1.57E-15$
8	$4.11E-03$	$4.61E-02$	$2.16E-15$	$1.28E-02$	$1.44E-01$	$3.19E-15$
16	$1.04E-03$	$2.33E-02$	$4.25E-15$	$3.25E-03$	$7.30E-02$	$6.28E-15$
32	$2.61E-04$	$1.17E-02$	$8.42E-15$	$8.18E-04$	$3.67E-02$	$1.31E-14$
Rate	2.00	1.00	–	1.99	0.99	–
$k = 2$						
N	$\|\boldsymbol{u} - \boldsymbol{u}_h\|$	$\|p - p_h\|$	$\|\nabla \cdot (\boldsymbol{u} - \boldsymbol{u}_h)\|$	$\|\boldsymbol{u} - \boldsymbol{u}_h\|$	$\|p - p_h\|$	$\|\nabla \cdot (\boldsymbol{u} - \boldsymbol{u}_h)\|$
4	$1.02E-03$	$6.36E-03$	$1.26E-14$	$2.91E-03$	$2.57E-02$	$6.10E-15$
8	$1.27E-04$	$1.58E-03$	$3.79E-14$	$3.67E-04$	$6.76E-03$	$1.23E-14$
16	$1.58E-05$	$3.84E-04$	$2.35E-14$	$4.63E-05$	$1.73E-03$	$2.47E-14$
32	$1.96E-06$	$9.41E-05$	$4.75E-14$	$5.82E-06$	$4.36E-04$	$4.98E-14$
Rate	3.00	2.02	–	2.99	1.99	–
$k = 3$						
N	$\|\boldsymbol{u} - \boldsymbol{u}_h\|$	$\|p - p_h\|$	$\|\nabla \cdot (\boldsymbol{u} - \boldsymbol{u}_h)\|$	$\|\boldsymbol{u} - \boldsymbol{u}_h\|$	$\|p - p_h\|$	$\|\nabla \cdot (\boldsymbol{u} - \boldsymbol{u}_h)\|$
4	$2.14E-05$	$2.13E-04$	$9.71E-15$	$1.48E-04$	$1.53E-03$	$1.22E-14$
8	$1.35E-06$	$2.61E-05$	$1.88E-14$	$9.03E-06$	$1.90E-04$	$2.46E-14$
16	$8.43E-08$	$3.23E-06$	$3.76E-14$	$5.56E-07$	$2.36E-05$	$4.83E-14$
32	$5.27E-09$	$4.02E-07$	$7.35E-14$	$3.45E-08$	$2.95E-06$	$9.67E-14$
Rate	4.00	3.00	–	4.01	3.00	–

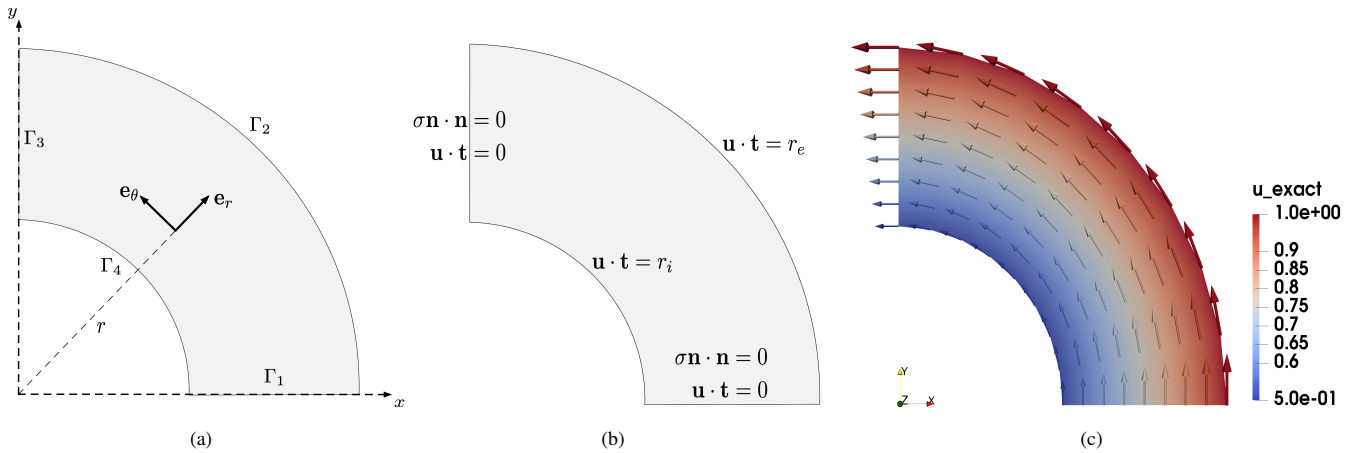

(a) (b) (c)

Figure 10 Curved domain problem: (a) geometry, (b) boundary conditions and (c) exact solution for the velocity magnitude, $\mathbf{u}_{exact}$.

The pressure exact solution is set zero in this case, $p_{exact} = 0$. This condition is weakly imposed by the term,

$$\langle \boldsymbol{\sigma n}, \boldsymbol{v} \rangle_{\partial\Omega_N} = 0, \tag{45}$$

having in mind that $\nabla \boldsymbol{u} + \nabla \boldsymbol{u}^T = 0$ for the radial velocity field solution, thus $\boldsymbol{\sigma n} = (2\mu D(\boldsymbol{u}) - pI)\boldsymbol{n} = -p\boldsymbol{n}$.

The mesh geometry is build with the same number of divisions N in the angular $\boldsymbol{e}_\theta$ and radial $\boldsymbol{e}_r$ directions. The procedure is repeated for triangular meshes, using N_r divisions in the radial direction $\boldsymbol{e}_r$, and N_θ in the angular direction $\boldsymbol{e}_\theta$. These partitions are illustrated in Fig. 11.

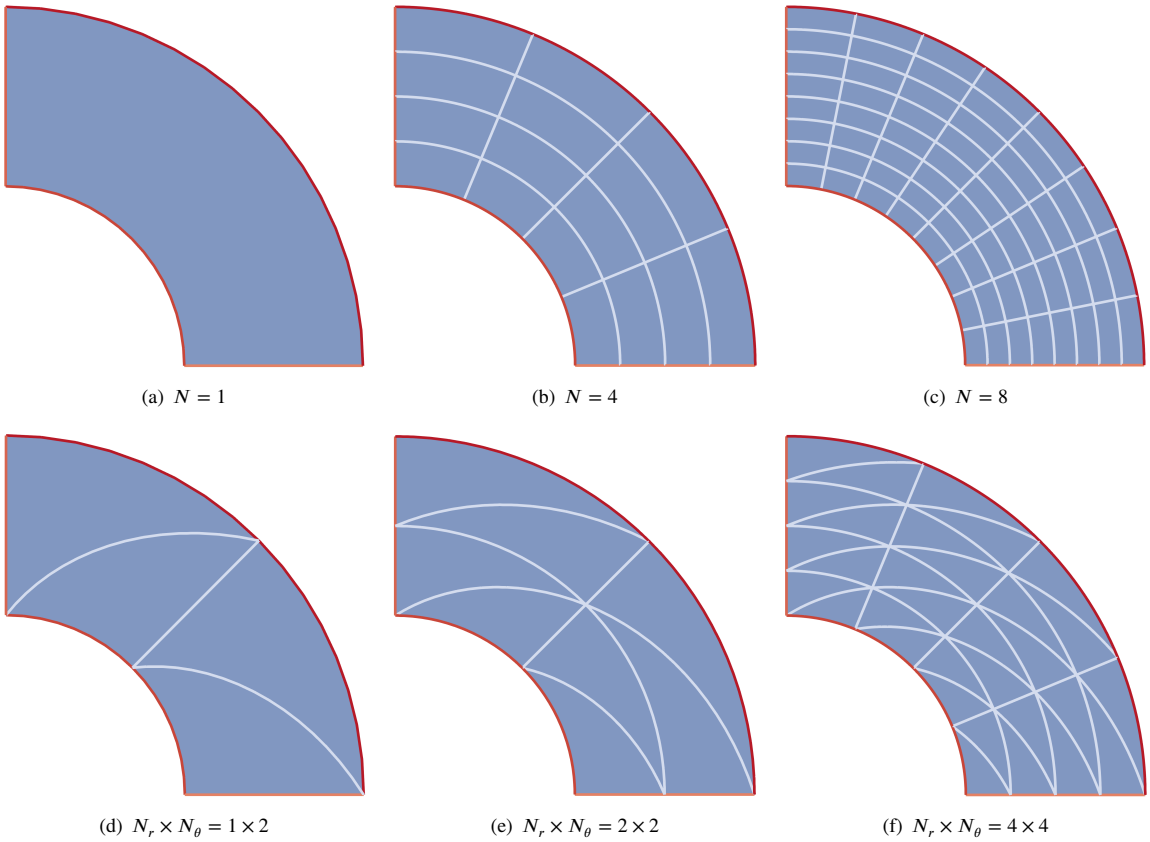

(a) $N = 1$ (b) $N = 4$ (c) $N = 8$

(d) $N_r \times N_\theta = 1 \times 2$ (e) $N_r \times N_\theta = 2 \times 2$ (f) $N_r \times N_\theta = 4 \times 4$

Figure 11 Curved domain problem: curved quadrilateral meshes with N divisions in $\boldsymbol{e}_\theta$ and $\boldsymbol{e}_r$ directions, and curved triangular meshes with $N_r \times N_\theta$ divisions.

The L^2-errors for $\boldsymbol{u}$, p and $\nabla \cdot \boldsymbol{u}$ are shown in Table 7 for quadrilateral and triangular elements, using the space configurations $S_{h,RT(k)}$ and $S_{h,BDM^+(k)}$, respectively, with approximation orders $k = 1$ and 2. The error magnitude obtained indicates that the approximation reaches exactly the solution of the problem.

In Fig. 12, for quadrilateral mesh elements with $N = 4$ divisions, we compare linear and non-linear transformations for the gradient of velocity shape functions, and their implications in the pressure field solutions. As observed in Fig. 12(b), the approximation of the pressure has a reduced error and recovers the exact solution, when the derivative of the directions vector is computed, following the expression (40).

6.4.3 | Flow in a domain with obstacles

At this point, the study is focused on the movement of a fluid ($\mu = 1$) through circular obstacles, arranged in a square domain $\Omega = (0.0, 2.0) \times (0.0, 2.0)$, as shown in Fig. 13(a). A unit normal flux is injected through the left boundary (Dirichlet condition). The slip condition, $\boldsymbol{\sigma n} \cdot \boldsymbol{t} = 0$, with no penetration, $\boldsymbol{u} \cdot \boldsymbol{n} = 0$, is set in the obstacles, bottom and top boundaries. For the problem well-posedness, the Neumann boundary condition, $\boldsymbol{\sigma n} \cdot \boldsymbol{n} = 0$, is applied to the right face.

The simulations are done for 4×4 obstacles, with diameter $D = 0.25$, in case 1; and 8×8 obstacles, with $D = 0.125$, in case 2. The mesh refinement pattern is represented in Fig. 13(b) for the 4×4 obstacles case. In order to build the curved elements of the mesh, the procedure described in Section 5.2 is employed. The hybrid formulation uses space configuration $S_{h,RT(k)}$ with approximation order $k = 2$.

In Figs. 14 and 15, the solutions for velocity and pressure are displayed, respectively, for the 4×4 obstacles domain ($D = 0.25$). The same is done in Figs. 16 and 17, for the 8×8 obstacles domain ($D = 0.125$).

We observe in the graphics of pressure, that the Stokes problem over obstacles has an approximate behavior of a flow in porous media. In Figs. 15 and 17, as the number of obstacles increases (and their diameters decrease), the pressure drop approaches a

Table 7 Stokes problem in curved region: errors in $\boldsymbol{u}$, p and $\nabla \cdot \boldsymbol{u}$, measured in L^2-norms, obtained with the space configurations $S_{h,RT(k)}$ and $S_{h,BDM^+(k)}$ based on curved quadrilateral and triangular meshes, respectively, using $k = 1, 2$.

Curved quadrilateral elements				Curved triangular elements			
$k = 1$							
N	$\|\boldsymbol{u} - \boldsymbol{u}_h\|$	$\|p - p_h\|$	$\|\nabla \cdot (\boldsymbol{u} - \boldsymbol{u}_h)\|$	$N_r \times N_\theta$	$\|\boldsymbol{u} - \boldsymbol{u}_h\|$	$\|p - p_h\|$	$\|\nabla \cdot (\boldsymbol{u} - \boldsymbol{u}_h)\|$
1	$1.82E-16$	$5.61E-16$	$3.41E-16$	1×2	$2.39E-16$	$2.16E-15$	$7.63E-16$
4	$2.37E-16$	$2.74E-15$	$6.79E-16$	2×2	$2.02E-16$	$3.67E-15$	$5.11E-16$
8	$5.77E-16$	$4.68E-15$	$1.32E-15$	4×4	$2.45E-16$	$5.64E-15$	$9.26E-16$
$k = 2$							
N	$\|\boldsymbol{u} - \boldsymbol{u}_h\|$	$\|p - p_h\|$	$\|\nabla \cdot (\boldsymbol{u} - \boldsymbol{u}_h)\|$	$N_r \times N_\theta$	$\|\boldsymbol{u} - \boldsymbol{u}_h\|$	$\|p - p_h\|$	$\|\nabla \cdot (\boldsymbol{u} - \boldsymbol{u}_h)\|$
1	$1.97E-16$	$1.24E-15$	$7.83E-16$	1×2	$3.57E-16$	$1.35E-14$	$2.49E-15$
4	$1.98E-16$	$2.01E-15$	$1.31E-15$	2×2	$2.44E-16$	$1.15E-14$	$1.67E-15$
8	$4.41E-16$	$1.28E-14$	$5.08E-15$	4×4	$2.70E-16$	$1.12E-14$	$2.26E-15$

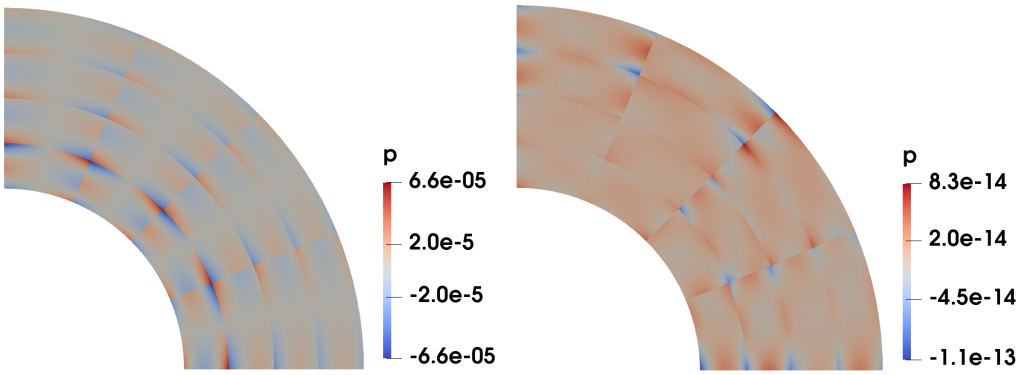

(a) (b)

Figure 12 Quadrilateral meshes for a curved domain, $N = 4$: pressure field results with (a) linear and (b) non-linear gradient transformation.

linear behavior. Therefore, the obstacles domain can be replaced by a permeability coefficient, and the flow can be described by a Darcy flow equation. In the sequence, a verification procedure is proposed.

A permeability coefficient, compatible with the obstacle region, can be calculated based on the pressure difference between left and right extremity points of the domain, in the flux direction. The pressure drops $\Delta p_{num} = 167.00$ and $\Delta p_{num} = 680.00$ are obtained for the cases 1 and 2, respectively.

These values are applied to the Darcy's law equation, considering a volumetric flow rate $Q = 1/2$ and the flow distance $\Delta l = 2$, in order to obtain the numerical permeability coefficient κ_{num}:

$$\kappa_{num} = Q\frac{\Delta l}{\Delta p_{num}} = \frac{1}{\Delta p_{num}}. \tag{46}$$

For verification, this permeability is compared with an estimated coefficient κ by the homogenization procedure suggested in[54], where different curves are plotted for the parameters: $\varepsilon = 1 - \frac{\pi d^2}{4S^2}$ and $\kappa^* = \frac{\kappa}{d^2}$, related to geometrical properties of the obstacles (where S is the distance between two obstacles center points). In Table 8, κ and κ_{num} values are compared for the cases 1 and 2 with obstacle diameters D.

The results of the comparative study shown in Table 8 indicates that the permeability values κ_{num} represent a good approximation for κ, that is to say, the pressure drop in the obstacles domain varies close to the linear profile verified by Darcy law.

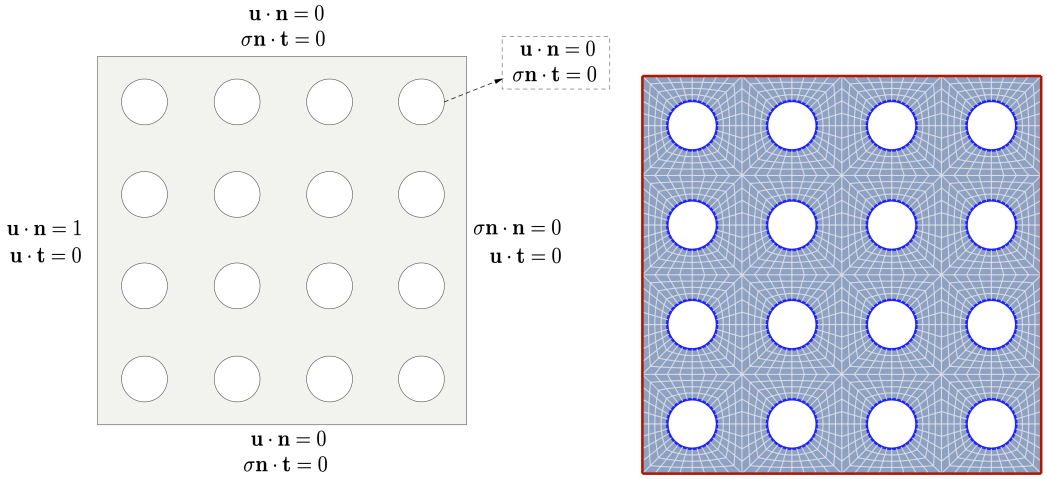

Figure 13 Flow past obstacles problem : (a) boundary conditions and (b) mesh refinement pattern, 4×4 obstacles.

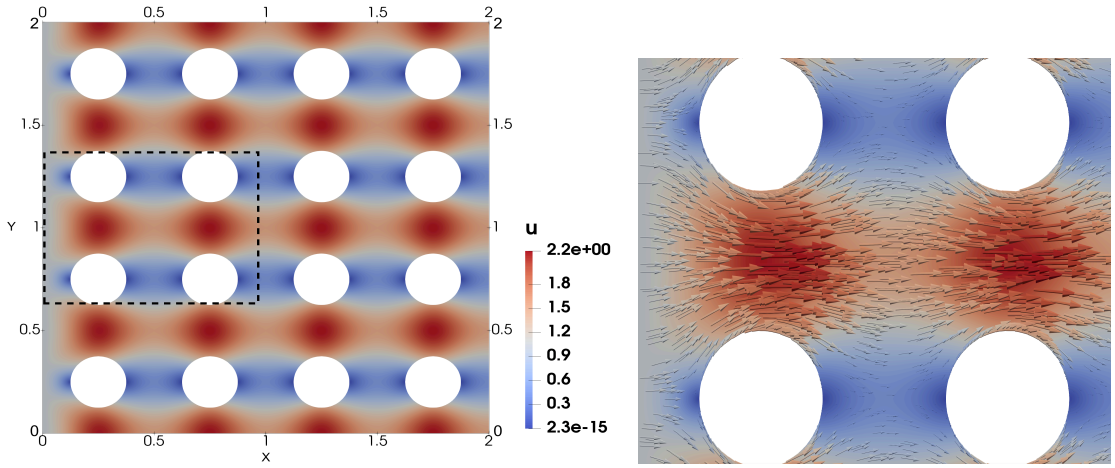

Figure 14 Stokes flow over obstacles: velocity solution, 4×4 obstacles with $D = 0.25$.

Table 8 Comparative study of permeability coefficients κ_{num} (corresponding to Δp_{num}) and κ [54], for obstacle diameters D.

D	0.25	0.125
κ	0.00625	0.00156
κ_{num}	0.00599	0.00147
Δp_{num}	167.00	680.00

7 | APPLICATION TO COUPLED STOKES-DARCY PROBLEMS

Let us consider a two-dimensional Stokes-Darcy model consisting of a Stokes problem for a fluid in the domain Ω_f that can flow across an interface $\Gamma_{fp} = \Omega_f \cap \Omega_p$ into a saturated porous medium domain Ω_p, both regions forming the computational domain $\Omega = \Omega_f \cup \Omega_p$, as graphically represented in Figure 18.

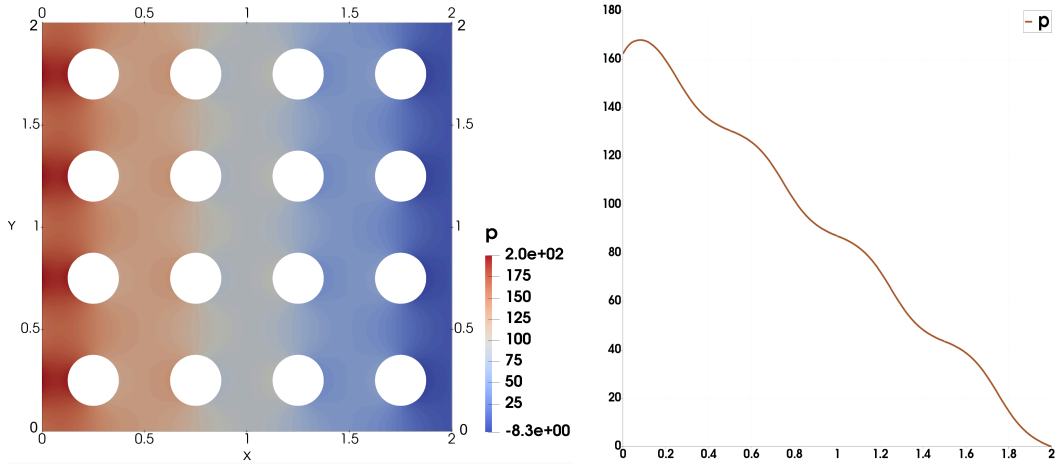

Figure 15 Stokes flow over obstacles: pressure solution, 4×4 obstacles with $D = 0.25$. Pressure drop in $y = 1$.

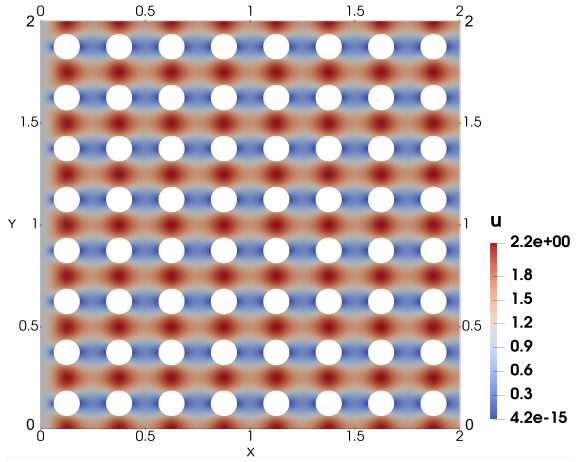

Figure 16 Stokes flow over obstacles: velocity solution, 8×8 obstacles with $D = 0.125$.

The velocity $\boldsymbol{u} = (\boldsymbol{u}_f, \boldsymbol{u}_p)$ and pressure $p = (p_f, p_p)$ fields are identified by the corresponding index f (for free-fluid) or p (for porous medium). The variables $(\boldsymbol{u}_f, p_f)$ and $(\boldsymbol{u}_p, p_p)$ verify the Stokes equations

$$-\underline{\nabla} \cdot \boldsymbol{\sigma}(\boldsymbol{u}_f, p_f) = \boldsymbol{f}, \quad \nabla \cdot \boldsymbol{u}_f = 0, \quad \text{in} \quad \Omega_f, \tag{47}$$

and the Darcy law equations

$$\mathbb{K}^{-1}\boldsymbol{u}_p + \nabla p_p = 0, \quad \nabla \cdot \boldsymbol{u}_p = 0 \quad \text{in} \quad \Omega_p. \tag{48}$$

For the examples to be simulated the viscosity $\mu > 0$ is constant in Ω_f and constant permeability tensor $\mathbb{K} = \gamma\mathbb{I}$ in Ω_p, $\gamma > 0$ are adopted.

To complete the problem, interface and boundary conditions need to be imposed. The interface conditions at $\Gamma_{fp} = \Omega_f \cap \Omega_p$ are

$$\boldsymbol{u}_f \cdot \boldsymbol{n}_f + \boldsymbol{u}_p \cdot \boldsymbol{n}_p = 0 \quad \text{Flux continuity} \tag{49}$$

$$-2\mu \left[D(\boldsymbol{u}_f)\boldsymbol{n}_f\right] \cdot \boldsymbol{n}_f + p_f = p_p \quad \text{Balance of normal forces} \tag{50}$$

$$-2 \left[D(\boldsymbol{u}_f)\boldsymbol{n}_f\right] \cdot \tau_{fd} = \alpha_{BJS}\, \boldsymbol{u}_f \cdot \tau_{fp} \quad \text{(BJS) condition,} \tag{51}$$

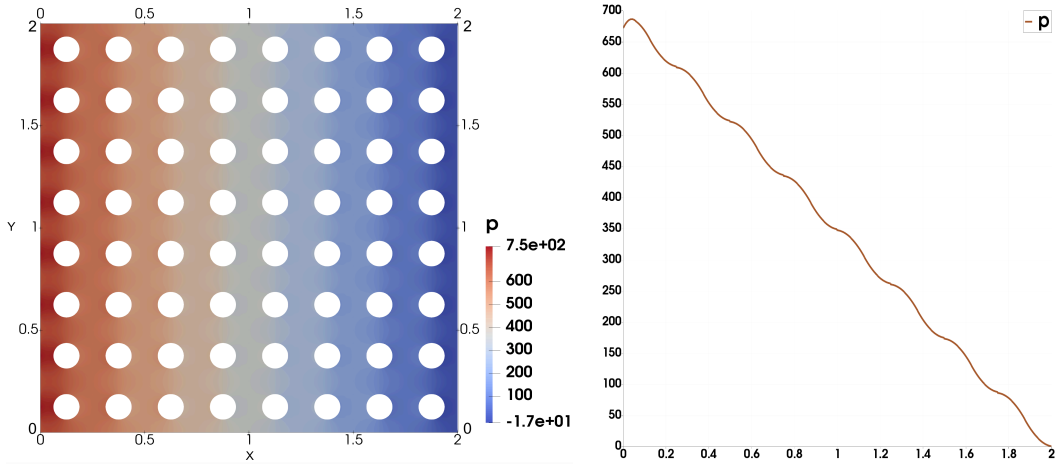

Figure 17 Stokes flow over obstacles: pressure solution, 8×8 obstacles with $D = 0.125$. Pressure drop in $y = 1$.

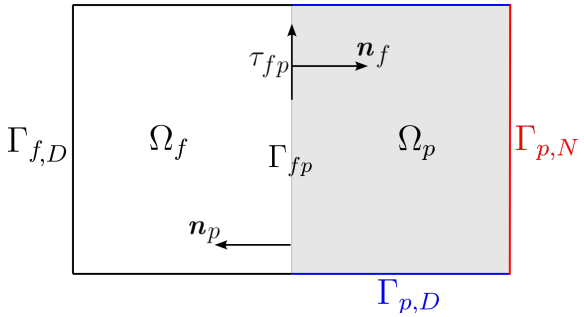

Figure 18 Coupling problem scheme: fluid domain Ω_f, porous medium Ω_p and coupling interface Γ_{fp}.

where τ_{fd} is a unit tangent vector field on Γ_{fp}, $\boldsymbol{n}_f$ and $\boldsymbol{n}_p$ being the unit normal vectors pointing outwards from Ω_f and Ω_p. The parameter $\alpha_{BJS} > 0$ is a friction coefficient (in practice, it is obtained from experimental data[55]).

$$\boldsymbol{u}_f = \boldsymbol{u}_D \quad \text{on} \quad \Gamma_{f,D}, \tag{52}$$

$$\boldsymbol{u}_p \cdot \boldsymbol{n}_p = \theta_N \quad \text{on} \quad \Gamma_{p,N}, \quad p_p = p_D \quad \text{on} \quad \Gamma_{p,D}, \tag{53}$$

where $\Gamma_{f,D} = \partial\Omega_f \setminus \Gamma_{fp}$ and $\Gamma_{p,N} \cup \Gamma_{p,D} = \partial\Omega_p \setminus \Gamma_{fp}$. When $\Gamma_{pD} = \emptyset$, these boundary conditions require the compatibility constraints $(g, 1)_{\Omega_p} = 0$, and $(p, 1)_\Omega = 0$. Moreover, in the applications to be simulated, θ_N is taken as a piecewise constant function.

Semi-Hybrid-mixed FE method for the Stokes-Darcy problem

We propose a discretization of the aforementioned coupled Stokes-Darcy problem by adopting a mixed method for the porous media flow in Ω_d and a semi-hybrid-mixed model for the approximation of the Stokes equations, following similar steps presented in previous sections for Stokes problems. Precisely,

1. Construction of shape regular and conformal partitions for the flow domains, $\mathcal{T}_{h,f} = \{K_f\}$ and $\mathcal{T}_{h,p} = \{K_p\}$, such that the conglomerate partition $\mathcal{T}_h = \mathcal{T}_{h,f} \cup \mathcal{T}_{h,p}$ of Ω is conformal along the interface Γ_{fp}.

2. For the hybridization of the Stokes model, set the mesh skeleton Γ_f formed by the edges of the elements $K_f \in \mathcal{T}_{h,f}$ not included in Γ_{fp}.

3. Definition of a divergence-compatible FE pair $\boldsymbol{X}_h \times \Psi_h \subset \boldsymbol{X} \times \Psi$ based on $\mathcal{T}_h$, and of $\boldsymbol{X}_h(\theta_N) = \{\boldsymbol{v} = (\boldsymbol{v}_f, \boldsymbol{v}_p) \in \boldsymbol{X}_h; \boldsymbol{v}_p \cdot \mathbf{n}_p|_{\Gamma_{pN}} = \theta_N\}$.

4. Definition of a FE trace space $\boldsymbol{\Lambda}^t_{f,h}$ based on $\Gamma_f \cup \Gamma_{fp}$ verifying the trace compatibility condition with respect to $\boldsymbol{X}_{h,f} = \boldsymbol{X}_h|_{\Omega_f}$.
5. The Beavers–Joseph–Saffman is weakly enforced using a Lagrange multiplier $\boldsymbol{\lambda}^t_h|_{\Gamma_{fp}} \approx -[\boldsymbol{\sigma}\boldsymbol{n}_f]\cdot\boldsymbol{\tau}_{fp} = -2\mu[D(\boldsymbol{u})\boldsymbol{n}_f]\cdot\boldsymbol{\tau}_{fp} = \alpha_{BJS}\,\boldsymbol{u}_f\cdot\boldsymbol{\tau}_{fp}$.
6. Definition of the FE setting $\mathcal{S}^{fp}_h(\theta_N) = \boldsymbol{X}_h(\theta_N)\times\Psi_h\times\boldsymbol{\Lambda}^t_{f,h}$ (or $\mathcal{S}^{fp}_h(\theta_N) = \boldsymbol{X}_h(\theta_N)\times\Psi_{h0}\times\boldsymbol{\Lambda}^t_{f,h}$, if $\Gamma_{pD} = \emptyset$).

Observe that the flux continuity (49) is directly obtained from the H(div)-conforming property of the FE space $\boldsymbol{X}_h$. Moreover, the balance of normal forces in (50) leads us to the definition of the bilinear form in $\boldsymbol{X}_h$:

$$a^{fp}_h(\boldsymbol{u},\boldsymbol{v}) := 2\mu\sum_{K_f\in\mathcal{T}_{h,f}}(D(\boldsymbol{u}_f),D(\boldsymbol{v}_f))_{K_f} + \sum_{K_p\in\mathcal{T}_{h,p}}(\mathbb{K}^{-1}\boldsymbol{u}_p,\boldsymbol{v})_{K_p}.$$

Based on the above setting, we propose a semi-hybrid-mixed FE method for the coupled Stokes-Darcy problem (47)-(51) expressed in the form:

HM-H(div)($\mathcal{S}^{fp}_h(\theta_N)$): find $(\boldsymbol{u}_h, p_h, \boldsymbol{\lambda}^t_h)\in\mathcal{S}^{fp}_h(\theta_N)$ satisfying for all $(\boldsymbol{v}, q, \boldsymbol{\eta}^t)\in\mathcal{S}^{fp}_h(0)$:

$$a^{fp}_h(\boldsymbol{u}_h,\boldsymbol{v}) + b(\boldsymbol{v},p_h) + \langle\boldsymbol{\lambda}^t_h,\boldsymbol{v}\rangle_{\Gamma_f} + \langle\boldsymbol{\lambda}^t_h,\boldsymbol{v}\rangle_{\Gamma_{fp}} = \langle\boldsymbol{v}\cdot\boldsymbol{n}_p, p_D\rangle_{\Gamma_{p,D}} + (\boldsymbol{f},\boldsymbol{v})_{\Omega_f}, \tag{54}$$

$$b(\boldsymbol{u}_h,q) = -(g,q)_{\Omega_p}, \tag{55}$$

$$\langle\boldsymbol{\eta}^t,\boldsymbol{u}_h\rangle_{\Gamma_f} - \alpha^{-1}_{BJS}\langle\boldsymbol{\eta}^t,\boldsymbol{\lambda}^t_h\rangle_{\Gamma_{fp}} + \langle\boldsymbol{\eta}^t,\boldsymbol{u}_h\rangle_{\Gamma_{fp}} = \langle\boldsymbol{\eta}^t,\boldsymbol{u}_D\rangle_{\Gamma_{f,D}}, \tag{56}$$

Remark 5. Observe that:

- The additional variable $\rho\in\mathbb{R}$ used in Stokes-Brinkman problems to enforce the pressure zero-mean constraint is not required for coupled-Darcy problems.
- The application of static condensation in system (54)-(56) follows a procedure similar to the one described in Section 5.1 for Stokes-Brinkman problems. Namely, it requires the introduction of two new variables $\bar{p}_h\in\bar{\mathcal{P}}_h$ and $\bar{g}_h\in\bar{\mathcal{P}}_h$, playing the roles of element average pressure and element distributed flux, respectively. In this way, the primary variable $V_1 = (\bar{p}_h, \underline{u}_e, \boldsymbol{\lambda}^t_h)$ is solved by a global system and the secondary variables $V_2 = (V_{f,2}, V_{p,2})$ are recovered in each element $K_f\in\mathcal{T}_{h,f}$ and $K_p\in\mathcal{T}_{h,p}$, respectively. The independent local solvers are determined by the corresponding method adopted in each flow region: the new semi-hybrid mixed solver in the Stokes region Ω_f and the standard mixed formulation for Darcy flows in the porous media Ω_p.

7.1 | Convergence verification

Consider the Stoke-Darcy model proposed in[56] for a free-flow domain $\Omega_f = (0,\pi)\times(0,1)$ on top of the porous medium domain $\Omega_p = (0,\pi)\times(-1,0)$. Taking constant permeability $\mathbb{K} = \mathbb{I}$, unit parameters $\mu = \alpha = \alpha_{BJS} = 1$, the functions

$$\boldsymbol{u}_f = \begin{bmatrix} v'(y)\cos x \\ v(y)\sin x\end{bmatrix},\quad p_f = \sin x\,\sin y,\quad \text{where}\quad v(y) = \frac{1}{\pi^2}\sin^2(\pi y) - 2, \tag{57}$$

$$\boldsymbol{u}_p = \begin{bmatrix} (e^{-y}-e^{y})\cos x \\ -(e^{-y}+e^{y})\sin x\end{bmatrix},\quad p_p = (-e^{-y}+e^{y})\sin x. \tag{58}$$

are exact solutions. The corresponding sources $g = 0$ and $\mathbf{f}$, the boundary data $\boldsymbol{u}_D$ on $\Gamma_{f,D}$, and θ_N on $\Gamma_{p,N} = \partial\Omega_p\setminus\Gamma_{fp}$ are extracted from these analytical expressions.

In this section, the new semi-hybrid-mixed formulation (54)-(56) is verified for this problem using FE space settings of types $\mathcal{S}^{fp}_{h,RT(k)}(\theta_N)$ and $\mathcal{S}^{fp}_{h,BDM^+(k)}(\theta_N)$ applied on uniform quadrilateral and triangular meshes $\mathcal{T}_h$, respectively, with mesh size $h = 2^{1-N}, N = 2^i, i = 2,\cdots 6$.

The resulting L^2-errors for $\boldsymbol{u} = (\boldsymbol{u}_f,\boldsymbol{v}_p)$, $\nabla\cdot\boldsymbol{u} = (\nabla\cdot\boldsymbol{u}_f, \nabla\cdot\boldsymbol{u}_p)$, and $p = (p_f, p_p)$ are shown in Table 9 for each flow regime. Namely, data for the free-flow are listed on the left side, and for the porous media flow they are on the right side.

Optimal convergence rates of order $k+1$ occur for $\boldsymbol{u}_p$, $\nabla\cdot\boldsymbol{u}_p$ and p_p in the porous domain Ω_p, as in standard applications of the mixed method for Darcy flows based on divergence-compatible FE pairs of $RT(k)$ or $BDM^+(k)$ types.

In the Stokes domain, convergence for $\boldsymbol{u}_f$ and p_f is in accordance with the numerical studies for the HM-H(div)($S_{h,RT(k)}$) and HM-H(div)($S_{h,BDM^+(k)}$) formulations presented in the previous sections for pure Stokes flows, including the divergence-free property for $\boldsymbol{u}_f$.

The errors shown in Table 9 for the HM-H(div)($S_{RT(k)}$) method are plotted in Figure 19. For comparison, corresponding error curves given by the symmetric Discontinuous Galerkin method $RT^{\text{div},DG}(k)$ are included as well. The two methods give similar convergence histories, in both flow regions, specially for increasing polynomial degree.

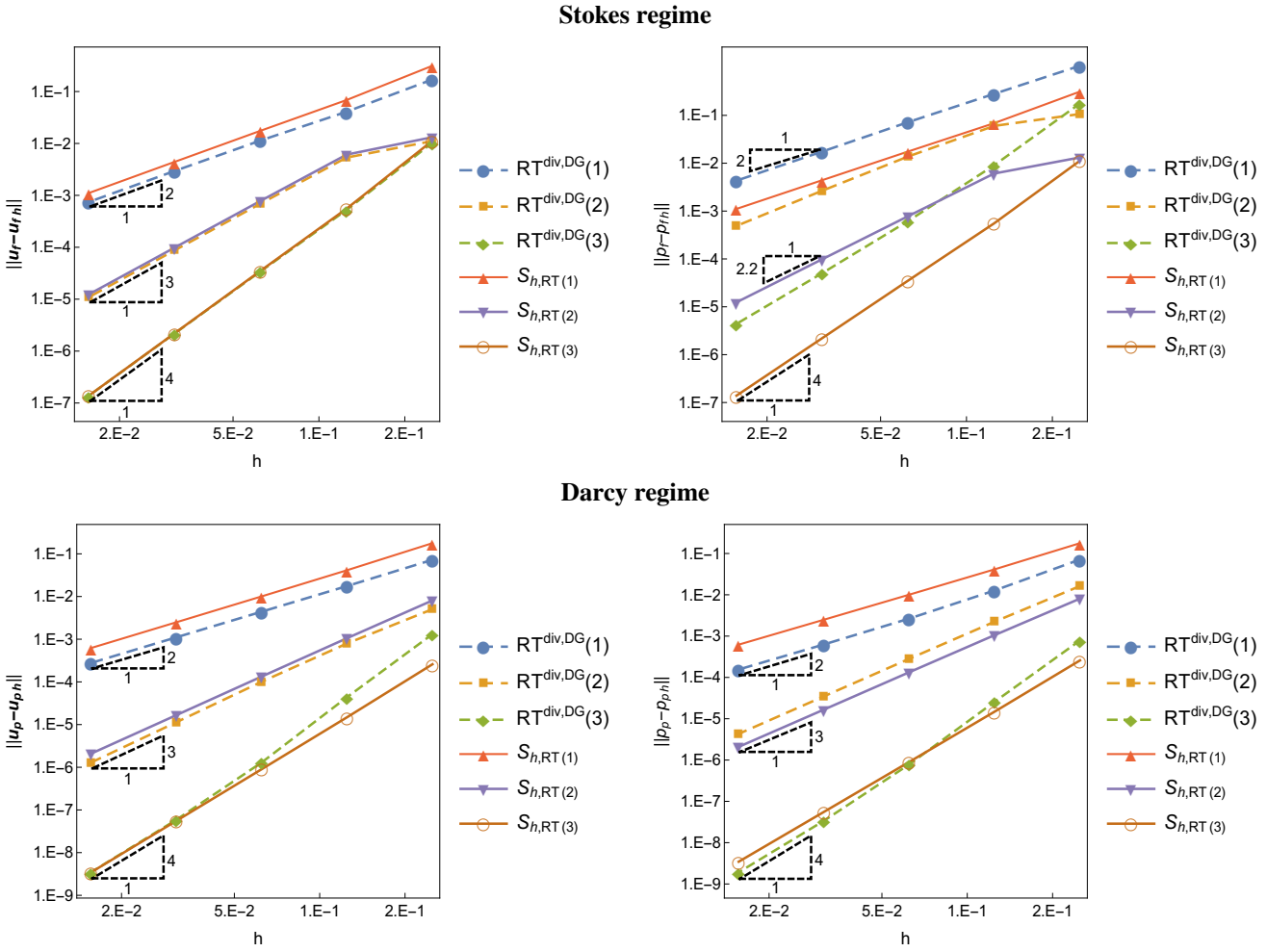

Figure 19 Stokes-Darcy problem: convergence history for $\boldsymbol{u}_{fh}$ (left side) and p_{fh} (right side) in the Stokes regime, obtained with symmetric DG methods $RT^{\text{div},DG}(k)$ and HM-H(div)($S_{h,RT(k)}$) formulations based on quadrilateral meshes, for $k = 1, 2$ and 3(top); Similar error curves for $\boldsymbol{u}_{ph}$ and p_{ph} (down) in the Darcy subdomain.

7.2 | Application to a carbonate karst reservoir

The numerical study of this section is for a two-dimensional carbonate karst reservoir model composed of multiple vugs with different shapes and sizes in a rectangular domain $\Omega = (0, 3) \times (0, 2)$, as illustrated in Figure 20. The free-flow region Ω_f is composed by the vugs, which are surrounded by a porous medium Ω_p. Since $\partial\Omega_f \cap \partial\Omega = \emptyset$, then $\Gamma_{fp} = \partial\Omega_f$. The Neumann boundary datum is: $\theta_N = 0$ on bottom and top horizontal sides of Ω, inlet $\theta_N = 1$ on the left vertical side. Dirichlet condition $p_p = 0$ is enforced on the right vertical side. The parameters $\mu = 0.1$ and $\alpha_{BJS} = 1$ are considered, and the diagonal permeability tensor $\mathbb{K} = 0.5\mathbb{I}$ is taken in Ω_p. Vanishing source terms $g = 0$ and $\mathbf{f} = \mathbf{0}$ are applied.

Table 9 L^2-errors in $\boldsymbol{u} = (\boldsymbol{u}_f, \boldsymbol{v}_p)$, $p = (p_f, p_p)$, and $(\nabla \cdot \boldsymbol{u}_f, \nabla \cdot \boldsymbol{u}_p)$ of the solution (57)-(58) for the Stokes-Darcy coupled problem approximated by the HM-H(div)($\mathcal{S}_{h,RT(k)}$) and HM-H(div)($\mathcal{S}_{h,BDM^+(k)}$) methods based on uniform quadrilateral and triangular meshes $\mathcal{T}_h$, $h = 2^{1-N}$.

Quadrilateral elements: $\mathcal{S}^{fp}_{h,RT(k)}(\theta_N)$						
N	$\|\boldsymbol{u}_f - \boldsymbol{u}_{fh}\|$	$\|p_f - p_{fh}\|$	$\|\nabla \cdot (\boldsymbol{u}_f - \boldsymbol{u}_{fh})\|$	$\|\boldsymbol{u}_p - \boldsymbol{u}_{ph}\|$	$\|p_p - p_{ph}\|$	$\|\nabla \cdot (\boldsymbol{u}_p - \boldsymbol{u}_{ph})\|$
	$k = 1$					
4	$3.14E-01$	$2.40E-01$	$2.19E-15$	$1.78E-01$	$8.05E-02$	$4.03E-15$
8	$6.86E-02$	$4.95E-02$	$4.37E-15$	$4.14E-02$	$1.96E-02$	$1.47E-14$
16	$1.76E-02$	$1.30E-02$	$8.00E-15$	$1.01E-02$	$4.88E-03$	$5.31E-14$
32	$4.43E-03$	$3.30E-03$	$1.60E-14$	$2.50E-03$	$1.22E-03$	$1.89E-13$
64	$1.11E-03$	$8.27E-04$	$3.33E-14$	$6.22E-04$	$3.05E-04$	$7.81E-13$
Rate	2.00	2.00	–	2.01	2.00	–
N	$k = 2$					
4	$1.32E-02$	$2.10E-02$	$5.96E-15$	$8.10E-03$	$2.72E-03$	$9.40E-15$
8	$6.09E-03$	$5.98E-03$	$1.44E-14$	$1.06E-03$	$3.38E-04$	$3.63E-14$
16	$7.85E-04$	$9.85E-04$	$2.64E-14$	$1.34E-04$	$4.23E-05$	$1.36E-13$
32	$9.89E-05$	$1.90E-04$	$5.24E-14$	$1.67E-05$	$5.28E-06$	$5.67E-13$
64	$1.24E-05$	$4.26E-05$	$1.09E-13$	$2.09E-06$	$6.61E-07$	$2.16E-12$
Rate	3.00	2.15	–	3.00	3.00	–
N	$k = 3$					
4	$1.13E-02$	$9.02E-03$	$1.63E-14$	$2.59E-04$	$1.23E-04$	$3.82E-14$
8	$5.54E-04$	$4.46E-04$	$3.78E-14$	$1.49E-05$	$7.64E-06$	$1.12E-13$
16	$3.54E-05$	$2.87E-05$	$6.70E-14$	$9.05E-07$	$4.78E-07$	$3.58E-13$
32	$2.22E-06$	$1.82E-06$	$1.40E-13$	$5.58E-08$	$2.99E-08$	$1.16E-12$
64	$1.39E-07$	$1.16E-07$	$3.00E-13$	$3.46E-09$	$1.87E-09$	$4.50E-12$
Rate	4.00	3.97	–	4.01	4.00	–

Triangular elements: $\mathcal{S}^{fp}_{h,BDM^+(k)}(\theta_N)$						
N	$\|\boldsymbol{u}_f - \boldsymbol{u}_{fh}\|$	$\|p_f - p_{fh}\|$	$\|\nabla \cdot (\boldsymbol{u}_f - \boldsymbol{u}_{fh})\|$	$\|\boldsymbol{u}_p - \boldsymbol{u}_{ph}\|$	$\|p_p - p_{ph}\|$	$\|\nabla \cdot (\boldsymbol{u}_p - \boldsymbol{u}_{ph})\|$
	$k = 1$					
4	$1.92E-01$	$9.38E-01$	$1.75E-15$	$1.35E-01$	$7.36E-02$	$4.61E-15$
8	$5.47E-02$	$4.62E-01$	$2.76E-15$	$3.50E-02$	$1.94E-02$	$9.07E-15$
16	$1.50E-02$	$2.31E-01$	$7.62E-15$	$9.02E-03$	$4.96E-03$	$2.26E-14$
32	$3.86E-03$	$1.16E-01$	$2.41E-14$	$2.28E-03$	$1.25E-03$	$9.63E-14$
64	$9.74E-04$	$5.78E-02$	$4.80E-14$	$5.72E-04$	$3.13E-04$	$3.82E-13$
Rate	1.99	1.00	–	1.99	2.00	–
N	$k = 2$					
4	$2.09E-02$	$1.16E-01$	$6.46E-15$	$9.29E-03$	$4.59E-03$	$1.31E-14$
8	$4.14E-03$	$6.66E-02$	$1.28E-14$	$1.18E-03$	$5.70E-04$	$2.67E-14$
16	$5.29E-04$	$1.67E-02$	$2.75E-14$	$1.46E-04$	$7.11E-05$	$7.13E-14$
32	$6.67E-05$	$4.06E-03$	$6.19E-14$	$1.64E-05$	$8.88E-06$	$2.91E-13$
64	$8.37E-06$	$9.94E-04$	$1.35E-13$	$1.86E-06$	$1.11E-06$	$1.28E-12$
Rate	2.99	2.03	–	3.14	3.00	–
N	$k = 3$					
4	$8.04E-03$	$8.25E-02$	$2.57E-14$	$2.47E-03$	$3.41E-04$	$3.39E-14$
8	$4.72E-04$	$9.17E-03$	$5.21E-14$	$1.10E-04$	$1.62E-05$	$8.25E-14$
16	$2.80E-05$	$1.12E-03$	$9.52E-14$	$4.48E-06$	$9.64E-07$	$2.28E-13$
32	$1.68E-06$	$1.38E-04$	$1.59E-13$	$2.01E-07$	$6.00E-08$	$7.34E-13$
64	$1.04E-07$	$1.72E-05$	$3.59E-13$	$9.86E-09$	$3.75E-09$	$2.30E-12$
Rate	4.02	3.01	–	4.35	4.00	–

The HM-H(div)($S_{h,BDM^+(k)}$) method for $k = 2$ is adopted, based on a triangular mesh created by the finite element mesh generator *Gmsh*, composed of 11422 nodes and 195665 elements.

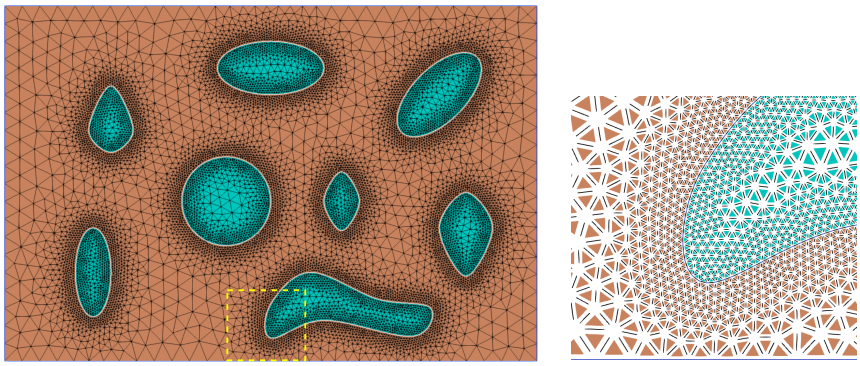

Figure 20 Triangular mesh refinement of a vuggy porous media and a zoom in of the marked region.

The resulting numerical results are plotted in Figs. 21 for the velocity magnitude $\boldsymbol{u}(x, y)$ and the pressure $p(x, y)$ fields. In the velocity field solution, the streamlines show that the vug surfaces affect the flow direction and penetration. Considering this horizontal inlet flow, we observe that velocity magnitudes inside a vug decrease as the vug dimension in the flow direction is larger than the other one.

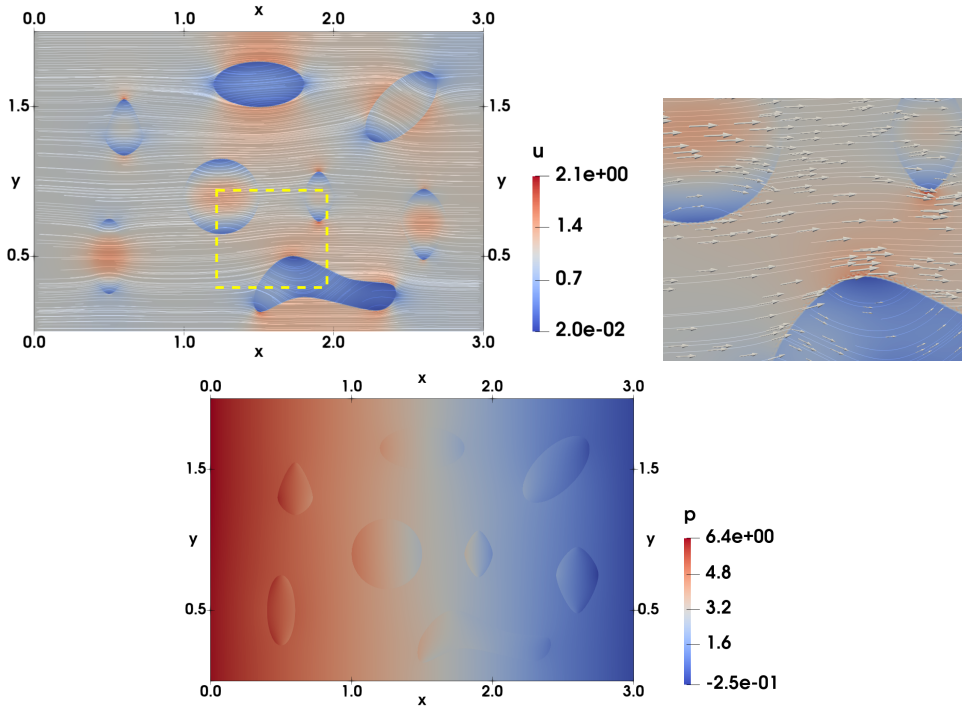

Figure 21 Stokes-Darcy problem with multiple vugs: numerical results for the magnitude of velocity/flux field $\boldsymbol{u}(x, y)$ and a zoom in view of the marked region (top images); pressure field $p(x, y)$ (bottom image).

8 | CONCLUSIONS

A numerical scheme for approximating Stokes, Brinkman and/or coupled Stokes-Darcy equations is presented. The core feature of the scheme is the use of divergence-compatible pairs of FE spaces in H(div)-L^2 to approximate the fluid velocity and pressure. The continuity of the tangential velocity is weakly enforced by a Lagrange multiplier variable. In this sense, the method can be seen as a semi-hybrid mixed formulation.

The approximations are pointwise mass conservative. From the theoretical point of view, we were able to demonstrate the solvability of the proposed scheme under a trace compatibility constraint, which was numerically verified for some classic H(div)-L^2 FE pairs. The hybridization of stable nonconforming methods proposed in the literature reveal that stability of the tangent velocity approximation can be obtained by increasing the internal polynomial order of approximation.

We also consider the method for a Stokes-Darcy coupling, where the term modeled by Beaver-Joseph-Saffman is elegantly approximated adding an L^2 product term in the tangent velocity space.

The numerical results of the application of the proposed method to problems with known solutions verify convergence, pressure robustness and a smooth transition for the Darcy limit of the Brinkman problem. When compared to discontinuous Galerkin approximations using the same H(div)-L^2 FE pairs, the proposed scheme gives similar convergence results. Moreover, in the semi-hybrid mixed method a large number of degrees of freedom can be statically condensed resulting in a smaller global system of equations.

Efforts to obtain rigorous a priori error estimates, more general stability analyses, and to extend the technique to three dimensions are under development.

Acknowledgments

The authors thankfully acknowledge financial support from grant 2015/00373-7, ANP-Petrobras; grant 01P-4376/2015, The Brazilian Federal Agency for Support and Evaluation of Graduate Education (CAPES); grants 305425/2013-7, 304029/2013-0, 305823-2017-5 and 306167/2017-4, The National Council for Scientific and Technological Development (CNPq); grants #2016/05155 and #2016/13637-5, São Paulo Research Foundation (FAPESP). We also express our gratitude to EPIC—Energy Production Innovation Center, hosted by the University of Campinas (Unicamp) and sponsored by Equinor Brazil. And the grants #2017/15736-3 and #2022/16636-0, São Paulo Research Foundation (FAPESP), that partially supported this work.

Data Availability Statement

The data that support the findings of this study are available from the corresponding author upon reasonable request.

References

1. Slattery JC. *Advanced transport phenomena*. Cambridge University Press . 1999.

2. Girault V, Raviart PA. *Finite element methods for Navier-Stokes equations: theory and algorithms*. 5. Springer Science & Business Media . 2012.

3. Brezzi F. On the existence, uniqueness and approximation of saddle-point problems arising from lagragian multipliers. *R.A.I.R.O. Anal. Numer.* 1974; 8(R2): 129–151.

4. Boffi D, Brezzi F, Fortin M. *Mixed and hybrid finite element methods*. New York: Springer-Verlag . 2013.

5. Crouzeix M, Raviart PA. Conforming and non-conforming finite element methods for solving the stationary Stokes equations. *R.A.I.R.O Anal. Numér* 1973; 7(R-3): 33–76.

6. Brenner SC. Forty Years of the Crouzeix-Raviart Element. *Numer. Methods Partial Differential Equations* 2015; 31: 367-396.

7. Toselli A. hp discontinuous Galerkin approximations for the Stokes problem. *Mathematical Models and Methods in Applied Sciences* 2002; 12(11): 1565–1597.

8. Girault V, Rivière B, Wheeler M. A discontinuous Galerkin method with nonoverlapping domain decomposition for the Stokes and Navier-Stokes problems. *Mathematics of Computation* 2005; 74(249): 53–84.

9. Lazarov R, Ye X. Stabilized discontinuous finite element approximations for Stokes equations. *Journal of Computational and Applied Mathematics* 2007; 198(1): 236–252.

10. Zhao L, Sun S. A strongly mass conservative method for the coupled Brinkman-Darcy flow and transport. *arXiv:2112.05943* 2021.

11. Wang J, Wang Y, Ye X. A robust numerical method for Stokes equations based on divergence-free H(div) finite element methods. *SIAM Journal on Scientific Computing* 2009; 31(4): 2784-2802.

12. Könnö J, Stenberg R. H(div)-conforming finite elements for the Brinkman problem. *Mathematical Models and Methods in Applied Sciences* 2011; 21(11): 2227–2248.

13. Carvalho PG, Devloo PR, Gomes SM. On the use of divergence balanced H(div)-L2 pair of approximation spaces for divergence-free and robust simulations of Stokes, coupled Stokes-Darcy and Brinkman problems. *Mathematics and Computers in Simulation* 2020; 170: 51–78.

14. Mardal KA, Tai XC, Winther R. A robust finite element method for Darcy-Stokes flow. *SIAM Journal on Numerical Analysis* 2002; 40(5): 1605–1631.

15. Tai XC, Winther R. A discrete de Rham complex with enhanced smoothness. *Calcolo* 2006; 43(4): 287–306.

16. Xie X, Xu J, Xu G. Uniformly-stable finite element methods for Darcy-Stokes-Brinkman models. *Jounal of Computational Mathematics* 2008; 26(3): 437–455.

17. Guzmán J, Neilan M. A family of nonconforming elements for the Brinkman problem. *IMA Journal of Numerical Mathematics* 2012; 32(4): 1484–1508.

18. Chen SC, Dong LN, Qiao ZH. Uniformly convergent H(div)-conforming rectangular elements for Darcy–Stokes Problem. *Sci. China. Math.* 2013; 12: 2723-2736.

19. Chen SC, Dong LN, Zhao JK. Uniformly convergent cubic nonconforming element for Darcy–Stokes Problem. *J. Sci. Comput.* 2017; 72: 231-232.

20. Veubeke F. dB. Displacement and equilibrium models in the finite element method. *Stress analysis* 1965: chapter–9.

21. Arnold DN, Brezzi F. Mixed and nonconforming finite element methods: implementation, postprocessing and error estimates. *RAIRO* 1985; 19(1): 7–32.

22. Cockburn B, Nguyen NC, Peraire J. A comparison of HDG methods for Stokes flow. *Journal of Scientific Computing* 2010; 45(1-3): 215–237.

23. Egger H, Waluga C. hp analysis of a hybrid DG method for Stokes flow. *IMA Journal of Numerical Analysis* 2013; 33(2): 687-721.

24. Igreja I, Loula AFD. Stabilized velocity and pressure mixed hybrid DGFEM for the Stokes problem. *International Journal for Numerical Methods in Engineering* 2017; 112(7): 603–628.

25. Rhebergen S, Wells GN. Analysis of a hybridized/interface stabilized finite element method for the Stokes equations. *SIAM Journal on Numerical Analysis* 2017; 55(4): 1982–2003.

26. Rhebergen S, Wells GN. An embedded–hybridized discontinuous Galerkin finite element method for the Stokes equations. *Computer Methods in Applied Mechanics and Engineering* 2020; 358: 112619.

27. Cesmelioglu A, Rhebergen S, Wells GN. An embedded–hybridized discontinuous Galerkin method for the coupled Stokes–Darcy system. *Journal of Computational and Applied Mathematics* 2020; 367: 112476.

28. Di Pietro DA, Ern A, Lemaire S. An arbitrary-order and compact-stencil discretization of diffusion on general meshes based on local reconstruction operators. *Computational Methods in Applied Mathematics* 2014; 14(4): 461–472.

29. Araya R, Harder C, Poza AH, Valentin F. Multiscale hybrid-mixed method for the Stokes and Brinkman equations — the method. *Computer Methods in Applied Mechanics and Engineering* 2017; 324: 29–53.

30. John V, Linke A, Merdon C, M N, Rebholz L. On the divergence constraint in mixed finite element methods for incompressible flows. *SIAM Review* 2017; 59(3): 492-544.

31. Raviart PA, Thomas J. Primal hybrid finite element methods for 2nd order elliptic equations. *Mathematics of computation* 1977; 31(138): 391–413.

32. Roberts JE, Thomas JM. Mixed and Hybrid Methods. In: Ciarlet PG, Lions JL., eds. *Handbook of Numerical Analysis*. 2. Elsevier Science Publishers. 1991 (pp. 527-639).

33. Babuska I, Oden JT, Lee JK. Mixed-hybrid finite element approximations of second-order elliptic boundary-value problem. *Comput. Methods Appl. Mech. Engrg.* 1977; 11: 175–206.

34. Han HD. Nonconforming elements in the mixed finite element method. *J. Comput. Math* 1984; 2(3): 223-233.

35. Brezzi F, Douglas J, Marini LD. Two families of mixed finite elements for second order elliptic problems. *Numerische Mathematik* 1985; 47(2): 217–235.

36. Raviart P, Thomas JM. A mixed finite element method for 2-nd order elliptic problems. In: Lecture Notes in Mathematics 606, Springer. 1977 (pp. 292–315).

37. Brezzi F, Fortin M. *Mixed and hybrid finite element methods*. Springer-Verlag . 1991.

38. Farias AM, Devloo PRB, Siqueira dSMGD, Castro DA. Two dimensional mixed finite element approximations for elliptic problems with enhanced accuracy for the potential and flux divergence. *Computers & Mathematics with Applications* 2017; 74(9): 3283-3295.

39. Brezzi F, Douglas J, Duran R, Fortin M. Mixed finite elements for second order elliptic problems in three variables. *Numerische Mathematik* 1987; 51(2): 237–250.

40. Nédélec JC. Mixed finite elements in R^3. *Numerische Mathematik* 1980; 35(1): 315–341.

41. Castro DA, Devloo PR, Farias AM, Gomes SM, Durán O. Hierarchical high order finite element bases for H (div) spaces based on curved meshes for two-dimensional regions or manifolds. *Journal of Computational and Applied Mathematics* 2016; 301: 241–258.

42. Tai XC, Winter R. A discrete de Rham complex with enhanced smoothness. *Calcolo* 2007; 43(4): 287–306.

43. De Siqueira D, Devloo PR, Gomes SM. A new procedure for the construction of hierarchical high order Hdiv and Hcurl finite element spaces. *Journal of Computational and Applied Mathematics* 2013; 240: 204–214.

44. Castro DA, Devloo PRB, Farias AM, Gomes SM, D. DO. H(div) finite elements based on nonaffine meshes for 3D mixed formulations of flow problems with arbitrary high order accuracy of the divergence of the flux. *Journal of Computational and Applied Mathematics* 2016; 301: 241–258.

45. Calle JD, Devloo PRB, Gomes SM. Implementation of continuous hp-adaptive finite element spaces without limitations on hanging sides and distribution of approximation orders. *Comput. Math. Appl.* 2015; 70: 1051-1069.

46. Devloo PRB, Farias AG, Gomes SM, Siqueira dD. Two-dimensional hp adaptive finite element spaces for mixed formulations. *Mat. Comput. Simulat.* 2016; 126: 104-122.

47. Devloo PRB, Durán O, M GS, Shauer N. Mixed finite element approximations based on 3D *hp*-adaptive curved meshes with two types of H(div)-conforming spaces. *Int. J. Numer. Meth. Engnr.* 2017; 113(7): 1045-1060.

48. Siqueira dD, Farias AG, Devloo PRB, Gomes SM. Mixed finite element approximations of a singular elliptic problem based on some anisotropic and hp-adaptive curved quarter-point elements. *Appl. Num. Math.* 2020; 158: 85-102.

49. Duran O, Devloo PR, Gomes SM, Valentin F. A multiscale hybrid method for Darcy's problems using mixed finite element local solvers. *Computer Methods in Applied Mechanics and Engineering* 2019; 354: 213–244.

50. Botti L, Di Pietro DA, Droniou J. A Hybrid High-Order discretisation of the Brinkman problem robust in the Darcy and Stokes limits. *Computer Methods in Applied Mechanics and Engineering* 2018; 341: 278–310.

51. John V, Linke A, Merdon C, Neilan M, Rebholz LG. On the divergence constraint in mixed finite element methods for incompressible flows. *SIAM Review* 2017; 59(3): 492–544.

52. Devloo P, Durán O, Gomes S, Shauer N. Mixed finite element approximations based on 3-D hp-adaptive curved meshes with two types of H (div)-conforming spaces. *International journal for numerical methods in engineering* 2018; 113(7): 1045–1060.

53. Gordon WJ, Hall CA. Transfinite element methods: blending-function interpolation over arbitrary curved element domains. *Numerische Mathematik* 1973; 21(2): 109–129.

54. Tamayol A, Bahrami M. Analytical determination of viscous permeability of fibrous porous media. *International Journal of Heat and Mass Transfer* 2009; 52(9-10): 2407–2414.

55. Beavers GS, Joseph DD. Boundary conditions at a naturally permeable wall. *Journal of fluid mechanics* 1967; 30(01): 197–207.

56. Chen W, Wang F, Wang Y. Weak Galerkin method for the coupled Darcy–Stokes flow. *IMA Journal of Numerical Analysis* 2015; 36(2): 897–921.